

Breaking the Vicious Cycle: Coherent 3D Gaussian Splatting from Sparse and Motion-Blurred Views

Zhankuo Xu, Chaoran Feng, Yingtao Li, Jianbin Zhao, Jiashu Yang, Wangbo Yu,
Li Yuan[†], and Yonghong Tian[†], *Fellow, IEEE*

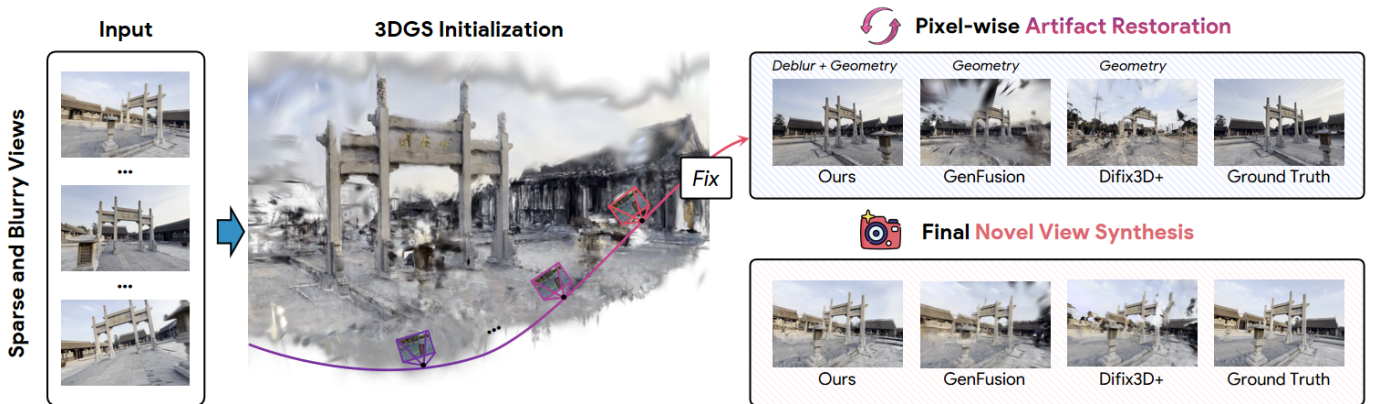


Fig. 1: We present **CoherentGS**, a novel 3D Gaussian Splatting (3DGS) framework for high-fidelity reconstruction from sparse and motion-blurred inputs. CoherentGS alternates between pixel-level artifact restoration and geometry completion guided by a dual prior: a deblurring prior that recovers high-frequency photometric detail and a diffusion prior conditioned on both 2D frames and 3D renderings to ensure cross-view consistency and 3D reconstruction quality.

Abstract—3D Gaussian Splatting (3DGS) has emerged as a state-of-the-art method for novel view synthesis. However, its performance heavily relies on dense, high-quality input imagery, an assumption that is often violated in real-world applications, where data is typically sparse and motion-blurred. These two issues create a vicious cycle: sparse views ignore the multi-view constraints necessary to resolve motion blur, while motion blur erases high-frequency details crucial for aligning the limited views. Thus, reconstruction often fails catastrophically, with fragmented views and a low-frequency bias. To break this cycle, we introduce CoherentGS, a novel framework for high-fidelity 3D reconstruction from sparse and blurry images. Our key insight is to address these compound degradations using a dual-prior strategy. Specifically, we combine two pre-trained generative models: a specialized deblurring network for restoring sharp details and providing photometric guidance, and a diffusion model that offers geometric priors to fill in unobserved regions of the scene. This dual-prior strategy is supported by several key techniques, including a consistency-guided camera exploration module that adaptively guides the generative process, and a depth regularization loss that ensures geometric plausibility. We evaluate CoherentGS through both quantitative and qualitative experiments on synthetic and real-world scenes, using as few as 3, 6, and 9 input views. Our results demonstrate that CoherentGS significantly outperforms existing methods, setting a new state-of-the-art for this challenging task. The code and video demos are available at <https://potatobigroom.github.io/CoherentGS/>.

Index Terms—3D Gaussian Splatting, Novel View Synthesis, Motion Deblurring, Sparse Viewpoints, Generative Model.

Z. Xu and C. Feng contributed equally to this work.

C. Feng, W. Yu, L. Yuan, and Y. Tian are with Peking University. Z. Xu, J. Zhao, J. Yang, and Y. Li are research interns at the School of Electronics and Computer Engineering, Peking University.

L. Yuan and Y. Tian are the corresponding authors (†). E-mail: {yuanli-ecce@pku.edu.cn, yhtian@pku.edu.cn}.

I. INTRODUCTION

Recently, 3D Gaussian Splatting (3DGS) [1] has emerged as an efficient and expressive scene representation, substantially advancing novel view synthesis (NVS). With dense multi-view coverage and sharp observations, 3DGS achieves high-fidelity reconstructions and has been rapidly adopted in a variety of applications [2]–[15]. However, such successes rely on input conditions that rarely hold in practice. In real-world scenarios, particularly in quick and unconstrained handheld/robot-mounted capture, image sequences are often sparse in viewpoints and degraded by motion blur. Under these conditions, the assumptions underpinning 3DGS break down: sparse views lead to fragmented local representations that fail to consolidate into a coherent global scene [16]–[19], while motion blur suppresses high-frequency details that are crucial for reliable geometry and texture recovery [20], [21]. When combined, these factors severely underconstrain optimization, making blur disentanglement particularly ill-posed and leading to severe degradation in reconstruction quality.

These challenges have two main consequences for 3D reconstruction: **view fragmentation** and **low-frequency bias**. Under sparse viewpoints, limited overlap weakens cross-view constraints and drives each camera to fit a localized distribution of Gaussian primitives rather than contributing to a coherent global representation; empirically, the learned distributions form fragmented clusters with weak cross-view overlap, leading to geometric drift and visible inconsistencies across views as shown in Fig. 2. Motion blur suppresses high-frequency cues such as textures and edges; instead of recovering these details, optimization typically reduces repro-

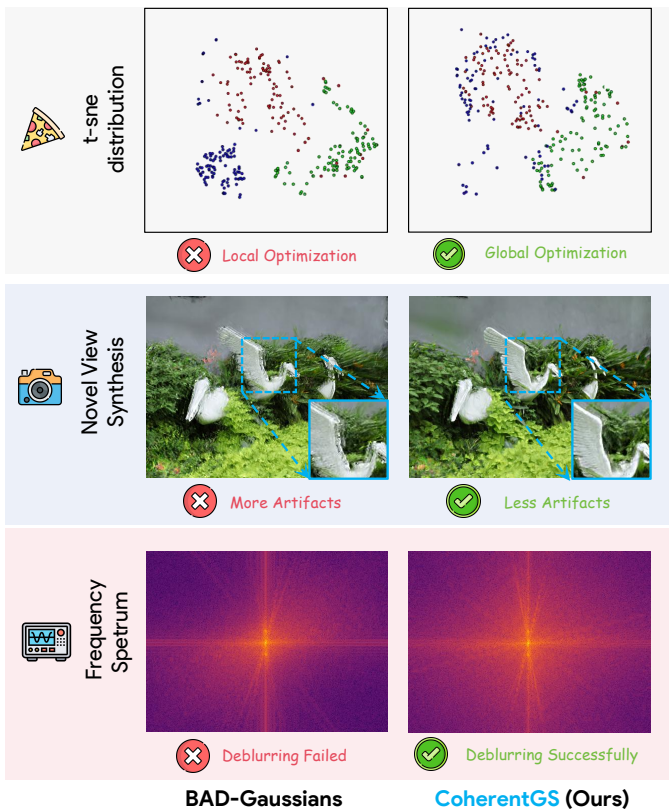


Fig. 2: **Visualizing view fragmentation.** We compare NVS and t-SNE distributions using only 3 input views. BAD-Gaussians [22] degenerates into fragmented local clusters, whereas CoherentGS maintains global geometric coherence.

jection error by inflating Gaussian covariances or blending colors, thereby fitting low-frequency signals at the expense of structural fidelity [23]–[25]. Fundamentally, fragmentation and low-frequency bias jointly exacerbate the ill-posedness: degenerate view-specific solutions explain blur via over-smoothed parameterizations, and the loss of high-frequency cues weakens geometric alignment across views. This vicious coupling leaves the problem severely underconstrained, preventing high-quality novel-view synthesis and stable scene-level coherence, consequently photorealistic supervision [1] and exposure modeling [5], [22], [26] alone are inadequate in this regime.

To address these challenges, we introduce a novel 3DGS-based reconstruction framework, **CoherentGS**. We posit that in the challenging real-world setting of sparse and blurry inputs, existing paradigms are insufficient. On one hand, state-of-the-art 3D deblurring methods [22], [27] excel at modeling camera motion but fundamentally rely on dense multi-view geometric constraints to decouple the trajectory from the scene. Under sparse views, these constraints vanish, causing the motion estimation to become ill-posed and the deblurring process to fail. On the other hand, while generative models can fill in missing content for sparse views, they are not specialized for physically-grounded deblurring and can hallucinate details inconsistent with the underlying motion. Therefore, our core insight is that *a robust solution must synergistically integrate two distinct, specialized priors: one for photometric deblurring*

and another for geometric completion.

Our CoherentGS framework employs this dual-prior strategy through a systematic and iterative process. The foundation of our method is a camera exposure motion model that explicitly simulates the blur formation by integrating multiple sharp 3DGS renderings along an optimized camera trajectory. To provide robust deblurring guidance, we distill knowledge from a pre-trained image deblurring model into our 3DGS representation using a perceptual distillation loss, which enforces the recovery of high-frequency details.

For scene-level geometric completion, we first propose a consistency-guided trajectory planner that identifies under-observed areas. A powerful diffusion model is then used to provide a supervisory signal for these novel views via a score distillation-inspired loss, ensuring contextual and geometric coherence. Finally, all components are optimized jointly within a unified framework: a composite objective combines a blurry reconstruction loss on real inputs with the two distillation losses from our generative priors, simultaneously refining the 3DGS scene and the camera motion parameters. This iterative loop of guided synthesis and joint optimization progressively enhances the scene’s completeness and high-frequency detail. We evaluate our method on the challenging Deblur-NeRF dataset [2] and proposed outdoor motion-blurred dataset. The experimental results demonstrate significant improvements over existing approaches and our contributions are summarized as follows:

- We introduce the first 3D Gaussian Splatting framework to systematically address the compound challenge of high-quality reconstruction from inputs that are simultaneously sparse and degraded by severe motion blur.
- We propose a novel dual-prior guidance strategy that integrates a generative diffusion model to resolve sparse-view ambiguities and a dedicated deblurring model to restore high-frequency details corrupted by motion.
- We develop a consistency-guided camera exploration for holistic and unseen view modeling, an exposure photometric bundle adjustment tailored for motion-blurred images, and a training scheme that jointly optimizes 3DGS with generated sequences.

II. RELATED WORK

A. 3D Representation from Degraded Images

Neural Radiance Fields (NeRF) [28] and 3D Gaussian Splatting (3DGS) [1] have emerged as powerful and novel 3D representations. However, their success is predicated on stringent input requirements, demanding both dense multi-view coverage and high-fidelity, blur-free imagery. In practical applications, these ideal conditions are seldom met, as captured images are often degraded. Consequently, reconstructing 3D scenes from such degraded inputs has become a critical and burgeoning area of research. Among various degradations, motion and defocus blur are particularly common in multi-view captures. Pioneering work in this domain focused on adapting NeRF to handle such artifacts. DeblurNeRF [2] was the first to jointly deblur and reconstruct a scene, modeling the blur kernel as a per-pixel ray transformation. Building on

this, subsequent methods sought to impose greater physical consistency; for instance, DP-NeRF [29] modeled the blur as a function of 3D rigid body motion, more closely approximating the physical camera capture process. Other notable contributions in this area include ExBluRF [30], PDRF [31], and their variants [26], [32]. With the advent of 3DGS, which offers efficient rendering and an explicit representation, the focus has shifted towards deblurring this new paradigm. Methods such as BAD-Gaussians [22], DeblurGS [33], Deblur3DGS [34], and others [35]–[38] have all proposed effective solutions, typically by explicitly modeling the camera’s motion trajectory during the exposure time to deconvolve the blur.

While previous methods have shown significant success, they often rely on the assumption that a relatively dense set of blurry images is available. However, this setup does not fully reflect the challenges encountered in real-world scenarios, where data can be both severely degraded and extremely limited. A more realistic and challenging situation arises when only a small number of images are available for a given scene, each suffering from motion blur [39]. We address this gap by tackling the combined problem of 3D reconstruction from inputs that are both sparse and blurry. We propose a framework that integrates deblurring techniques with strategies designed for sparse-view settings, thus improving the applicability of 3D reconstruction in real-world conditions.

B. Generative Priors for Novel View Synthesis.

Leveraging powerful and pre-trained generative models to overcome the limitations of 3D reconstruction from sparse or degraded imagery is a growing research area. This trend has largely branched into two specialized sub-domains targeting different types of degradation. The first and most prominent sub-domain addresses sparsity, where diffusion models are employed to rectify geometric and photometric deficiencies. Recent works including Difix3D+ [40], GSFixer [41], 3D-Enhancer [42] and [43]–[52] typically operate by rendering a flawed view, enhancing it with the diffusion prior, and distilling the refined details back into the 3D representation. On the other hand, some methods such as Sparse-DeRF [39] to tackle image blur, integrate specialized restoration networks to explicitly reverse the degradation process.

Despite their individual successes, these two paradigms have remained isolated. This separation presents a critical challenge: directly applying sparse-view generative methods to blurry inputs leads to hallucinated blur where the model mistakes artifacts for intrinsic texture, while applying deblurring networks to sparse data results in severe overfitting. Drawing inspiration from 2D knowledge distillation [53], our work is the first to bridge this gap by synergistically integrating distinct types of generative priors within a single, coherent optimization framework.

III. PRELIMINARY

A. 3D Gaussian Splatting

3DGS [1] explicitly represents the scene using a collection of sparse 3D Gaussians. Each primitive is parameterized by a 3D covariance matrix $\Sigma \in \mathbb{R}^{3 \times 3}$, a mean position $\mu \in \mathbb{R}^3$, an

opacity $o \in [0, 1]$, and spherical harmonics (SH) coefficients for view dependent color. The spatial influence of a Gaussian is defined as:

$$\mathcal{G}(\mathbf{x}) = \exp\left(-\frac{1}{2}(\mathbf{x} - \mu)^\top \Sigma^{-1}(\mathbf{x} - \mu)\right), \quad (1)$$

where Σ is factorized into a scaling matrix $\mathbf{S} \in \mathbb{R}^3$ and a rotation matrix $\mathbf{R} \in \text{SO}(3)$ to ensure positive semi-definiteness, formulated as $\Sigma = \mathbf{R}\mathbf{S}\mathbf{S}^\top\mathbf{R}^\top$. To render the scene from a specific viewpoint, the 3D covariance is projected into 2D image space as $\Sigma' = \mathbf{J}\mathbf{W}\Sigma\mathbf{W}^\top\mathbf{J}^\top$, where \mathbf{J} is the Jacobian of the affine projective approximation and \mathbf{W} is the viewing transformation matrix. The final pixel color C is computed by alpha blending N ordered primitives overlapping the pixel:

$$C = \sum_{i=1}^N T_i \alpha_i \mathbf{c}_i, \quad \text{with} \quad T_i = \prod_{j=1}^{i-1} (1 - \alpha_j), \quad (2)$$

where \mathbf{c}_i is the color derived from SH coefficients, and α_i denotes the final alpha contribution computed by multiplying the learned opacity o_i with the 2D Gaussian evaluation.

B. Image Blur Formation

The physical image formation process involves accumulating photons over a finite exposure period. Mathematically, this is modeled as the temporal integration of instantaneous sharp irradiance. Specifically, the motion blurred image $B(\mathbf{u})$ at pixel coordinate \mathbf{u} is formulated as:

$$B(\mathbf{u}) = \frac{1}{\tau} \int_0^\tau I(t, \mathbf{u}) dt, \quad (3)$$

where τ denotes the camera exposure duration, and $I(t, \mathbf{u})$ represents the instantaneous latent sharp image at time $t \in [0, \tau]$. The normalization factor $1/\tau$ ensures energy conservation during the integration window. For computational feasibility, we approximate this continuous integral using a discrete summation of n virtual sharp samples:

$$B(\mathbf{u}) \approx \frac{1}{n} \sum_{k=0}^{n-1} I_k(\mathbf{u}), \quad (4)$$

where $I_k(\mathbf{u})$ denotes the k^{th} virtual sharp instance sampled along the camera trajectory within the exposure interval.

C. Diffusion Model

Diffusion Models (DMs) are generative frameworks designed to approximate a data distribution $p_{\text{data}}(\mathbf{x})$ by reversing a gradual noise addition process. In the forward pass, an input sample \mathbf{x}_0 is progressively perturbed across discrete timesteps $t \in [0, T]$ by injecting Gaussian noise. This yields a noisy latent $\mathbf{x}_t = \alpha_t \mathbf{x}_0 + \sigma_t \epsilon$, where $\epsilon \sim \mathcal{N}(\mathbf{0}, \mathbf{I})$ is standard normal noise, and α_t, σ_t define the noise schedule. The generative reverse process utilizes a neural network \mathbf{F}_θ , termed the denoiser, to estimate the added noise. The parameters θ are optimized via a denoising score matching objective:

$$\mathcal{L}_{\text{DM}} = \mathbb{E}_{\mathbf{x}_0, t, \epsilon, \mathbf{c}} \left[\|\epsilon - \mathbf{F}_\theta(\mathbf{x}_t; t, \mathbf{c})\|_2^2 \right]. \quad (5)$$

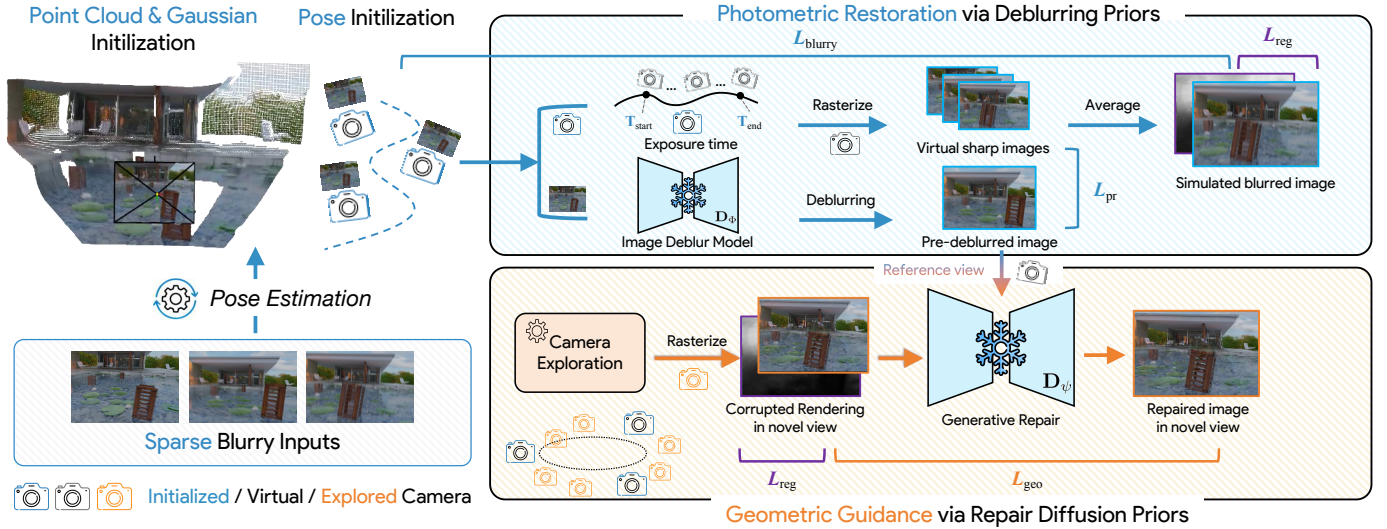


Fig. 3: **Overview of CoherentGS.** Our framework synergizes two generative priors to resolve sparse view ambiguity and motion blur. (Left) We initialize the Gaussian primitives using poses estimated by COLMAP [54]. (Top) Photometric Restoration via Deblurring Priors: This branch models the physical exposure trajectory to supervise blurry synthesis via $\mathcal{L}_{\text{blurry}}$ and distills sharp high frequency details from a pretrained deblurring network using a perceptual loss \mathcal{L}_{pr} . (Bottom) Geometric Guidance via Repair Diffusion Priors: This branch utilizes a diffusion model to repair structural defects in explorative viewpoints. A score distillation loss \mathcal{L}_{geo} and a depth regularization loss \mathcal{L}_{reg} are applied to guide the geometry completion and ensure consistency.

Here, the network \mathbf{F}_θ takes the noisy latent \mathbf{x}_t , the timestep t , and an optional condition vector \mathbf{c} (e.g., text embeddings or reference images) as input to reconstruct the signal. We employ this conditional generation capability to guide geometric completion in unobserved regions.

IV. METHOD

A. Problem Formulation and Overall Framework

Our **CoherentGS** framework employs a dual prior strategy to address the compound degradation of *view fragmentation* and *low frequency bias* inherent in motion blurred sparse view modeling, as depicted in Fig. 3. Given only a set of K sparse and blurry images $\{B_i\}_{i=1}^K$, we first establish an initial geometric backbone by estimating camera poses $\{\mathbf{T}_i\}_{i=1}^K$ by COLMAP [55] and initializing a 3DGS model \mathcal{G}_θ . The core of our method is an iterative loop designed to progressively enhance this initial reconstruction by synergistically applying two distinct generative priors. First, to address motion blur, we perform photometric restoration guided by a deblurring prior (Sec. IV-B). This module explicitly models the physical exposure trajectory to disentangle camera motion from scene appearance, thereby recovering high frequency details. Second, to resolve sparse view ambiguity, we introduce geometric completion guided by a conditional diffusion prior (Sec. IV-C). This process is steered by a consistency-guided camera exploration strategy (Sec. IV-D), which targets unobserved regions to steer the diffusion model in generating plausible geometric and contextual content. Finally, these two guidance mechanisms are integrated within a joint optimization scheme (Sec. IV-E), where the 3DGS model and camera parameters are updated using a composite loss that fuses supervision from the original blurry inputs with the signals from both generative

Algorithm 1 Photometric Restoration via a Deblurring Prior

- 1: **Function** ComputePerceptualLoss($\mathcal{G}_\theta, B_i, \mathbf{T}_{\text{start}}, \mathbf{T}_{\text{end}}$)
- 2: **Input:** Current 3DGS model \mathcal{G}_θ , a blurry input image B_i , and its corresponding start and end poses.
- 3: **Given:** Pre-trained deblurring model \mathbf{D}_Φ , pre-trained feature extractor Θ_{vgg} .
- 4: $\bar{I}_i \leftarrow \mathbf{D}_\Phi(B_i)$ \triangleright Eq. (9).
- 5: $F_{\text{target}} \leftarrow \Theta_{\text{vgg}}(\bar{I}_i)$
- 6: $\mathbf{T}_{\text{mid}} \leftarrow \text{InterpolatePose}(\mathbf{T}_{\text{start}}, \mathbf{T}_{\text{end}}, 0.5)$ \triangleright Eq. (6).
- 7: $\hat{I}_i \leftarrow \text{Render}(\mathcal{G}_\theta, \mathbf{T}_{\text{mid}})$
- 8: $F_{\text{render}} \leftarrow \Theta_{\text{vgg}}(\hat{I}_i)$
- 9: $\mathcal{L}_{\text{pr}} \leftarrow \|F_{\text{render}} - F_{\text{target}}\|_2^2$ \triangleright Eq. (10).
- 10: **Return** \mathcal{L}_{pr}

priors. This cyclical generation and reconstruction process is iterated to progressively refine the scene fidelity.

B. Photometric Restoration via Deblurring Prior

Our approach begins by explicitly modeling the physical process of motion blur as shown in Sec. III-B. The blur in a captured image B is the result of integrating light from a dynamic scene along a camera’s trajectory over its exposure time τ . We model this by optimizing a start pose $\mathbf{T}_{\text{start}}$ and an end pose \mathbf{T}_{end} for each capture. The latent camera pose \mathbf{T}_t at any time $t \in [0, \tau]$ is derived through linear interpolation in the SE(3) space:

$$\mathbf{T}_t = \mathbf{T}_{\text{start}} \cdot \exp\left(\frac{t}{\tau} \cdot \log(\mathbf{T}_{\text{start}}^{-1} \cdot \mathbf{T}_{\text{end}})\right). \quad (6)$$

By discretizing the exposure time into n samples, we can render a set of virtual sharp images $\{\hat{I}_i(\mathbf{T}_i, \theta)\}_{i=0}^{n-1}$ from the

3DGS model \mathcal{G}_θ . Averaging these sharp renderings allows us to synthesize a blurry image \hat{B} :

$$\hat{B}(\theta, \mathbf{T}_{\text{start}}, \mathbf{T}_{\text{end}}) = \frac{1}{n} \sum_{i=0}^{n-1} \hat{I}_i(\mathbf{T}_i, \theta). \quad (7)$$

This formulation allows us to supervise the 3DGS and the camera motion parameters using a photorealistic loss, $\mathcal{L}_{\text{blurry}}$, which measures the difference between the synthesized blurry image \hat{B} and the real captured image B :

$$\mathcal{L}_{\text{blurry}} = \lambda_1 \mathcal{L}_1(\hat{B}, B) + \lambda_{\text{SSIM}} \mathcal{L}_{\text{SSIM}}(\hat{B}, B). \quad (8)$$

However, under sparse-view conditions, relying solely on this blurry reconstruction loss is insufficient. The joint optimization of deblurring and 3D geometry becomes highly ill-posed, as there are not enough multi-view constraints to robustly decouple the camera motion from the scene’s appearance. A straightforward alternative would be to pre-deblur the input images and use them for direct pixel-wise supervision. This approach is prone to failure, as single-image deblurring is itself an ill-posed problem and applying it independently to multiple views often generates results that are not 3D-consistent, leading to severe geometric artifacts.

Inspired by [39], we address this by distilling knowledge from a powerful, pre-trained image deblurring model [56] in a robust feature space instead of the pixel space. First, we generate a set of target sharp images $\{\bar{I}_i\}_{i=1}^K$ by applying a pre-trained deblurring model \mathbf{D}_Φ to blurry inputs $\{B_i\}_{i=1}^K$:

$$\bar{I}_i = \mathbf{D}_\Phi(B_i). \quad (9)$$

Instead of enforcing strict pixel alignment with these pseudo-targets which may contain artifacts, we leverage them for high-level semantic guidance. We define a perceptual restoration loss \mathcal{L}_{pr} , that encourages the features of our rendered sharp image \hat{I}_i to match the features of the target deblurred image \bar{I}_i . To extract robust features, we employ a shared and pre-trained VGG [57] encoder Θ_{vgg} :

$$\mathcal{L}_{pr} = \|\Theta_{\text{vgg}}(\hat{I}_i) - \Theta_{\text{vgg}}(\bar{I}_i)\|_2^2. \quad (10)$$

For this formulation, the rendered sharp image \hat{I}_i is generated using the camera pose at the temporal midpoint $\mathbf{T}_{t=\tau/2}$, which serves as the canonical sharp state of the frame. This distillation mechanism provides strong priors for high-frequency details without enforcing strict pixel-level correspondence.

C. Geometric Guidance via Diffusion Prior

Recently, leveraging diffusion models to enhance 3DGS from limited inputs has gained significant attention. Recent works [40], [42], [43], [47] have shown that these models not only provide additional 3D priors for sparse views but also improve reconstruction quality by introducing high-frequency details. In this work, we integrate Difix3D+ [40] as our foundational generative prior to rectify structural defects. Specifically, it predicts a clean image \hat{I}_i^{fix} by conditioning on a reference view I_{ref} and the current noisy rendering \hat{I}_i :

$$\hat{I}_i^{\text{fix}} = \mathbf{D}_\psi(\hat{I}_i(\mathbf{T}_i, \theta); I_{\text{ref}}, t_0), \quad (11)$$

Algorithm 2 Geometric Guidance via Diffusion Prior

- 1: **Function** 3D-Consistency Distillation
 - 2: **Input:** Current 3DGS model \mathcal{G}_θ , camera pose \mathbf{T}_i , reference image I_{ref} from virtual viewpoint.
 - 3: **Given:** Pre-trained diffusion denoiser \mathbf{D}_ψ , noise schedule $\bar{\alpha}_t$, fixed timestep t_0 , feature extractor Θ_{vgg} .
 - 4: $\hat{I}_i \leftarrow \mathcal{G}_\theta(\mathbf{T}_i)$, $\mathbf{T}_i \in \{\mathbf{T}_i\}_{i=0}^{n-1}$ ▷ Eq. 6
 - 5: $t \leftarrow t_0$
 - 6: $\epsilon \sim \mathcal{N}(0, \mathbf{I})$
 - 7: $\hat{I}_{i,t} \leftarrow \sqrt{\bar{\alpha}_t} \hat{I}_i + \sqrt{1 - \bar{\alpha}_t} \epsilon$
 - 8: $\hat{I}_i^{\text{clean}} \leftarrow \mathbf{D}_\psi(\hat{I}_{i,t}; I_{\text{ref}}, t)$
 - 9: $\hat{I}_i^{\text{fix}} \leftarrow \text{sg}(\hat{I}_i^{\text{clean}})$
 - 10: $\mathcal{L}_{\text{geo}} \leftarrow \|\Theta_{\text{vgg}}(\text{sg}(\hat{I}_i^{\text{fix}})) - \Theta_{\text{vgg}}(\hat{I}_i)\|_2^2$ ▷ Eq. (12)
 - 11: **Return** \mathcal{L}_{geo}
-

Here, we sample a pre-deblurred image \bar{I}_j from Eq. 9 as reference image I_{ref} . However, directly utilizing these generative models presents a critical challenge in sparse-view scenarios where observations are severely degraded. A common approach is to reintroduce the generated images into the 3DGS training pipeline and apply a photorealistic loss for supervision. While this naive feedback loop improves sharpness, it introduces a diffusion bias by overemphasizing pixel-wise similarity, leading to over-smoothing and multi-view inconsistencies, especially in sparse regions.

To overcome this limitation, we propose a paradigm shift from using the diffusion model as an offline post-processor to leveraging it as an online supervisory signal via distillation.

Drawing inspiration from Score Distillation Sampling (SDS) [58], our method utilizes the pre-trained 2D diffusion model to provide informative gradients that guide the 3D optimization directly. Unlike the original noise-residual formulation in SDS, we adopt a more stable image-residual formulation.

The core objective is to guide the 3DGS to render images that the diffusion model perceives as structurally valid while maintaining semantic consistency. Specifically, we treat the single-step denoised output of the diffusion model as a pseudo-target and minimize its distance to the original 3DGS rendering. For each generated view, we formulate this geometric guidance loss as:

$$\mathcal{L}_{\text{geo}} = \lambda_{\text{geo}} \|\Theta_{\text{vgg}}(\text{sg}(\hat{I}_i^{\text{fix}})) - \Theta_{\text{vgg}}(\hat{I}_i)\|_2^2 \quad (12)$$

where \hat{I}_i is the image rendered from the current state of our 3DGS. $\hat{I}_i^{\text{fix}} = \mathbf{D}_\psi(\hat{I}_i; I_{\text{ref}}, t_0)$ is the predicted clean image after a single denoising step by the pre-trained Difix3D+ model, given the rendered image \hat{I}_i and reference image I_{ref} at a fixed timestep t_0 . The stop-gradient operator, $\text{sg}(\cdot)$, is crucial as it treats the diffusion model’s output as a fixed target, ensuring that gradients flow exclusively back to the 3DGS parameters θ . Following the official implementation of Difix3D+ configuration, we use a high-noise timestep by setting $t_0 = 199$. The detail is outlined in the Alg. 2

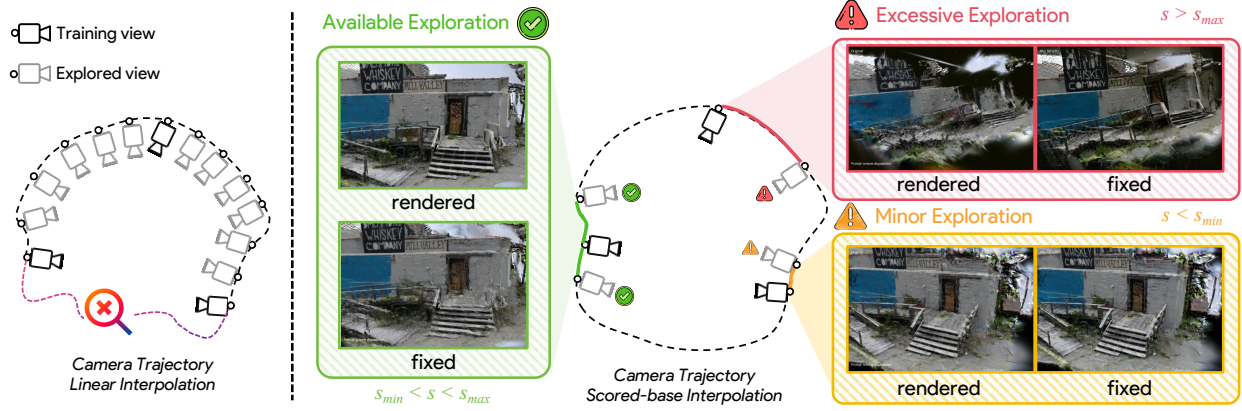


Fig. 4: **Comparison of different trajectories.** (Left) Linear interpolation between training views provides only limited angular diversity, often leading to ambiguous geometry. (Right) Our scored-based interpolation samples candidate poses along the $SE(3)$ geodesic and evaluates each with the diffusion-consistency score $\tilde{s}(\mathbf{T})$. Valid viewpoints ($s_{\min} \leq \tilde{s}(\mathbf{T}) \leq s_{\max}$) balance geometric diversity and diffusion stability, while excessive or minor exploration causes instability or redundancy. The proposed consistency-guided sampling adaptively expands recoverable viewpoints and enhances novel-view fidelity.

D. Consistency-guided Camera Exploration

The efficacy of the diffusion prior (Sec. IV-C) critically depends on the selection of viewpoints, where the rendered inputs must be informative enough to guide the geometry while remaining stable enough to prevent generative hallucinations. The primary challenge lies in exploring novel camera poses that maximize geometric supervision while maintaining structural plausibility. As illustrated in Fig. 4, naive linear interpolation between training views limits angular diversity and preserves geometric ambiguities. In contrast, large deviations from the image plane frequently result in loss of visual context and significant occlusions. To balance these conflicting factors, we propose a consistency-guided exploration strategy. This consistent-aware mechanism identifies and selects viewpoints that jointly provide high information gains and remain recoverable under the diffusion prior.

Scene Adaptive Consistency Normalization (SACN). The absolute scale of the generative consistency score is inherently scene dependent, fluctuating with exposure conditions and blur severity. To normalize the metric, we compute a per-scene baseline by averaging diffusion-aided consistency over all training views:

$$\bar{s} = \frac{1}{K} \sum_{i=1}^K \Theta_{\text{eval}}(\hat{I}^{\text{fix}}(\mathbf{T}_i), \hat{I}(\mathbf{T}_i)), \quad (13)$$

where Θ_{eval} is a pixel-wise evaluator, $\mathbf{T}_i \in \{\mathbf{T}_i\}_{i=1}^K$ are the training poses, $\hat{I}^{\text{fix}}(\mathbf{T}_i)$ is the denoised rendering, and $\hat{I}(\mathbf{T}_i)$ denotes the pose-specific reference.

Diffusion Reliability Metric. For each candidate pose \mathbf{T}_{new} , we quantify its diffusion consistency as

$$s(\mathbf{T}_{\text{new}}) = \Theta_{\text{eval}}(\hat{I}^{\text{fix}}(\mathbf{T}_{\text{new}}), \hat{I}(\mathbf{T}_{\text{new}})), \quad (14)$$

Here, a high score suggests the rendering deviates significantly from the diffusion prior, indicating potential artifacts or severe occlusions that the model cannot reliably repair. Conversely, an excessively low score implies the view is too similar to the training set or dominated by noise, offering negligible

Algorithm 3 Consistency-guided Camera Exploration

- 1: **Input:** Training poses $\{\mathbf{T}_i\}$, Reference images $\{\bar{I}_i\}$ \triangleright Eq. (9)
- 2: **Models:** 3DGS \mathcal{G}_θ , Diffusion Denoiser \mathbf{D}_ψ , Score function $S(\cdot)$
- 3: **Params:** Thresholds s_{\min}, s_{\max} , Interpolation $\text{interp}(\cdot)$
- 4: **Initialize:** Buffer $\mathcal{B}_{\text{gen}} \leftarrow \{\mathbf{T}_i\}$
- 5: **for each** adjacent pair $(\mathbf{T}_i, \mathbf{T}_{i+1})$ in \mathcal{B}_{gen} **do**
- 6: $\mathbf{T}_{\text{new}} \leftarrow \text{interp}(\mathbf{T}_i, \mathbf{T}_{i+1})$
- 7: $I_{\text{new}} \leftarrow \mathcal{G}_\theta(\mathbf{T}_{\text{new}})$
- 8: $I_{\text{fix}} \leftarrow \mathbf{D}_\psi(I_{\text{new}}, \bar{I}_i, t_0)$ \triangleright Eq. (11)
- 9: $s_{\text{curr}} \leftarrow S(I_{\text{fix}})$ \triangleright Eq. (15)
- 10: **if** $s_{\min} \leq s_{\text{curr}} \leq s_{\max}$ **then**
- 11: Add I_{fix} to training set
- 12: Add \mathbf{T}_{new} to \mathcal{B}_{gen}
- 13: **end if**
- 14: **end for**

geometric gradients. To derive a scene agnostic measure, we normalize it by the training baseline \bar{s} :

$$\tilde{s}(\mathbf{T}_{\text{new}}) = s(\mathbf{T}_{\text{new}}) - \bar{s}. \quad (15)$$

The normalized deviation $\tilde{s}(T)$ serves as a signal for recoverability, indicating how effectively the diffusion prior can refine the rendering without breaking geometric consistency.

Moderate deviations provide informative geometric cues with high reliability. In contrast, negligible deviations lead to redundant coverage, while excessive deviations risk inducing the unreliable hallucinations.

Band Pass View Selection. Candidate poses are generated by densely interpolating on the $SE(3)$ manifold between adjacent pairs $(\mathbf{T}_i, \mathbf{T}_{i+1})$, supplemented by minor extrapolation. This strategy introduces controlled viewpoint perturbations while ensuring the poses remain within vicinity of the observed trajectory. We retain candidates satisfying the band-pass criterion:

$$s_{\min} \leq \tilde{s}(\mathbf{T}) \leq s_{\max}. \quad (16)$$

The selected viewpoints are incorporated into the optimization loop, adapting the sampling budget toward under-constrained but recoverable regions. This targeted exploration progressively enhances novel-view fidelity and stabilizes diffusion-guided supervision with negligible computational overhead.

E. Joint Optimization with Reconstruction and Generation

The final stage of our framework involves jointly optimizing the 3D scene representation and the camera motion parameters as shown in Alg. 4. To achieve this, we formulate a composite objective function that integrates supervisory signals derived from both the raw blurry observations and the diffusion rectified novel views. This joint optimization allows the model to leverage the ground-truth constraints from the captured data while simultaneously benefiting from the strong generative prior to deblur and complete unseen regions.

To mitigate the inherent geometric ambiguity in sparse view reconstruction, we incorporate a depth regularization loss \mathcal{L}_{reg} inspired by RegNeRF [59]. This loss enforces a local smoothness prior on the rendered depth maps, which is critical for regularizing geometry in under-constrained and textureless regions. It effectively prevents degenerate solutions such as surface fragmentation and floating artifacts:

$$\mathcal{L}_{\text{reg}} = \sum_{i=0}^{n-1} \left(\|\nabla_x \hat{D}_i\|_1 + \|\nabla_y \hat{D}_i\|_1 \right) \quad (17)$$

By integrating these complementary supervisory signals, the total objective function $\mathcal{L}_{\text{total}}$ is formulated as a weighted sum of the reconstruction loss, the perceptual restoration loss, the geometric guidance loss, and the regularization term:

$$\mathcal{L}_{\text{total}} = \mathcal{L}_{\text{blurry}} + \lambda_{\text{pr}} \mathcal{L}_{\text{pr}} + \mathcal{L}_{\text{geo}} + \lambda_{\text{reg}} \mathcal{L}_{\text{reg}} \quad (18)$$

where λ_{pr} , λ_{geo} and λ_{reg} are scalar hyperparameters that balance the contribution of each term.

V. EXPERIMENTS

A. Implementation details

Dataset and preprocessing. We evaluate our method on the standard Deblur-NeRF benchmark [2], which comprises 5 synthetic and 5 real-world scenes characterized by severe motion blur. To further assess the generalization capability in complex, unconstrained outdoor environments, we establish a benchmark DL3DV-BLUR based on the DL3DV-10K dataset [60], simulating realistic motion blur across 5 diverse scenes. For experimental settings, we adopt sparse-view configurations with $K \in \{3, 6, 9\}$ views. We follow the train/test splitting protocol of BAD-Gaussians [22]: for the Deblur-NeRF dataset, we adopt the same train/test split as in their setting, while for the DL3DV-Blur dataset, we hold out every 7th image as the test set of novel views. More details of proposed dataset are in the *appendix*.

Evaluation metrics. We utilize several metrics to assess the quality of reconstruction and reenactment. The peak signal-to-noise ratio (PSNR), Structural Similarity (SSIM), and Learned Perceptual Image Patch Similarity (LPIPS) [61] are employed

Algorithm 4 Joint Optimization of CoherentGS

- 1: **Input:** Sparse, blurry images $\{B_i\}_{i=1}^K$.
 - 2: **Given:** Training iterations N_{iters} , generation interval N_{gen} , warmup iterations N_{warmup} .
 - 3: **Initialize:**
 - 4: Estimate initial poses $\{P_i\}_{i=1}^K$.
 - 5: Initialize 3DGS and motion θ , $\{\mathbf{T}_{\text{start},i}, \mathbf{T}_{\text{end},i}\}_{i=1}^K$.
 - 6: Initialize a buffer for generated views $\mathcal{B}_{\text{gen}} = \emptyset$.
 - 7: **for** iter = 1, ..., N_{iters} **do**
 - 8: // Phase 1: Generative Prior Expansion
 - 9: **if** iter % $N_{\text{gen}} == 0$ **and** iter $\geq N_{\text{warmup}}$ **then**
 - 10: $\Phi \leftarrow \text{PlanTrajectory}(\mathcal{G}_\theta, \{P_i\})$ ▷ Sec. IV-D
 - 11: $I_{\text{ref}} \leftarrow \text{Render from a training virtual pose.}$
 - 12: $\mathcal{S}_{\text{new}} \leftarrow \text{EnhanceViews}(\mathcal{G}_\theta, \Phi, I_{\text{ref}}, \mathbf{D}_\psi)$ ▷ Sec. IV-C
 - 13: Append new views \mathcal{S}_{new} to buffer \mathcal{B}_{gen} .
 - 14: **end if**
 - 15: // Phase 2: Reconstruction Optimization
 - 16: Sample a blurry image B_i and poses $\{\mathbf{T}_{\text{start},i}, \mathbf{T}_{\text{end},i}\}$.
 - 17: $\hat{B}_i \leftarrow \text{RenderBlurImage}(\mathcal{G}_\theta, \mathbf{T}_{\text{start},i}, \mathbf{T}_{\text{end},i})$ ▷ Eq. (7)
 - 18: $\mathcal{L}_{\text{blurry}} \leftarrow \text{ComputeLoss}(\hat{B}_i, B_i)$ ▷ Eq. (8)
 - 19: $\mathcal{L}_{\text{pr}} \leftarrow \text{ComputeLoss}(\mathcal{G}_\theta, B_i, \mathbf{T}_{\text{start},i}, \mathbf{T}_{\text{end},i})$ ▷ Eq. (10)
 - 20: **if** \mathcal{B}_{gen} is not empty **then**
 - 21: Sample a generated view $\{\hat{I}_j, \mathbf{T}_j, \hat{D}_j\}$ from \mathcal{B}_{gen} .
 - 22: $\mathcal{L}_{\text{geo}} \leftarrow \text{ComputeLoss}(\mathcal{G}_\theta, \hat{I}_j, I_{\text{ref}})$ ▷ Eq. (12)
 - 23: $\mathcal{L}_{\text{reg}} \leftarrow \text{ComputeLoss}(\hat{D}_j)$ ▷ Eq. (17)
 - 24: **else**
 - 25: $\mathcal{L}_{\text{geo}} \leftarrow 0, \mathcal{L}_{\text{reg}} \leftarrow 0$
 - 26: **end if**
 - 27: $\mathcal{L}_{\text{total}} \leftarrow \mathcal{L}_{\text{blurry}} + \lambda_{\text{pr}} \mathcal{L}_{\text{pr}} + \lambda_{\text{geo}} \mathcal{L}_{\text{geo}} + \lambda_{\text{reg}} \mathcal{L}_{\text{reg}}$
 - 28: Update θ , $\{\mathbf{T}_{\text{start},i}\}$, and $\{\mathbf{T}_{\text{end},i}\}$.
 - 29: **end for**
-

for evaluating image synthesis quality in novel view synthesis and deblurring view synthesis.

Training Details. Our framework is implemented based on the official implementation of BAD-Gaussians [22], incorporating the pre-trained prior from Difx3D+ [40]. We employ the Adam optimizer for all learnable parameters. The learning rate schedules and densification strategies for 3D Gaussian primitives strictly follow the default configuration in [1], [22]. For the camera trajectory modeling (Eq. (6)), the learning rates for translation and rotation ($T_{\text{start}}, T_{\text{end}}$) are initialized at 5×10^{-3} and exponentially decayed to 5×10^{-5} . The number of virtual camera poses n in (Eq. (7)) is set to 10. Regarding the loss terms, we set the blurry weight to $\lambda_1 = 0.8$, $\lambda_{\text{D-SSIM}} = 0.2$ and depth regularization weight $\lambda_{\text{reg}} = 0.1$. The weights for the deblurring (λ_{pr}) and geometric (λ_{geo}) priors are set to 0.01. To adapt to different scene distributions, the confidence thresholds for the score model are calibrated per dataset: we set $\{s_{\text{max}}, s_{\text{min}}\}$ to $\{14.5, 4.5\}$ for the outdoor DL3DV-Blur dataset, and $\{8.5, 2.5\}$ for the Deblur-NeRF dataset. The Θ_{eval} in (Eq. (13) and Eq. (14)) are defined as $\text{psnr}(\cdot)$. The training initiates with a warm-up phase of 1500 iterations dedicated to

TABLE I: Quantitative comparison of novel view synthesis on the synthetic dataset [2]. We compare the rendering quality with baselines given 3, 6, and 9 views. Each column is colored as: **best** and **second best**.

Method	PSNR \uparrow				SSIM \uparrow				LPIPS \downarrow			
	3-view	6-view	9-view	Average	3-view	6-view	9-view	Average	3-view	6-view	9-view	Average
BAD-Gaussians [22]	19.58	22.67	25.42	22.55	0.555	0.727	0.801	0.694	0.274	0.173	0.104	0.183
Sparse-DeRF* [39]	19.70	22.25	23.25	21.73	0.561	0.722	0.746	0.676	0.272	0.169	0.143	0.195
Difix3D+ [40]	18.43	19.14	19.74	19.11	0.504	0.551	0.584	0.547	0.307	0.287	0.275	0.289
GenFusion [47]	16.84	18.49	19.47	18.26	0.509	0.556	0.600	0.555	0.507	0.475	0.452	0.478
Ours	21.12	23.87	26.36	23.78	0.671	0.783	0.851	0.768	0.195	0.122	0.08	0.132



Fig. 5: **Qualitative results of novel view synthesis on Deblur-NeRF dataset.** We evaluate novel view synthesis performance against baseline methods under 3, 6, and 9 input view settings. Our approach consistently produces higher-fidelity renderings, recovering significantly more fine-grained details than competing methods.

the deblurring model. Subsequently, we incorporate diffusion prior and optimize under the guidance of the camera trajectory model, with the interpolation interval set to 200 steps. In total, the training spans a total of 7,000 iterations. All experiments are performed on a NVIDIA A6000 with 48GB memory. More training details are in the *appendix*.

Baselines. We benchmark our method against a comprehensive set of state-of-the-art approaches spanning two relevant domains. Specifically, to validate the reconstruction capability under sparse and blurry inputs, we compare our approach with BAD-Gaussians [22] and Sparse-DeRF¹ [39]. Furthermore, to

assess the performance of generative priors, we compare our method with recent 3D-aware generative models, including Difix3D+ [40] and GenFusion [47].

B. Experiment Results

Evaluation of Novel View Synthesis. We benchmark our method against state-of-the-art approaches, including GenFusion [47], Difix3D+ [40], and Sparse-DeRF [39]. As shown in Table I and Table III, CoherentGS achieves a great performance lead on the Deblur-NeRF dataset across all sparsity settings. Notably, in the most challenging 3-view scenario, our method outperforms GenFusion achieving a 4.28 dB gain in PSNR. This significant improvement underscores the efficacy

¹This method is not open-source, and we reproduct it based on DP-NeRF [29] and MPR-Net [56], denoted as Sparse-DeRF*.

TABLE II: **Quantitative comparison of novel view synthesis on proposed DL3DV-BLUR.** We compare the rendering quality with baselines given 3, 6, and 9 views. Each column is colored as: **best** and **second best**.

Method	PSNR \uparrow				SSIM \uparrow				LPIPS \downarrow			
	3-view	6-view	9-view	Average	3-view	6-view	9-view	Average	3-view	6-view	9-view	Average
BAD-Gaussians [22]	15.08	18.62	19.82	17.84	0.501	0.635	0.671	0.602	0.466	0.313	0.267	0.349
Sparse-DeRF* [39]	14.84	18.61	19.72	17.72	0.483	0.618	0.674	0.592	0.501	0.325	0.277	0.368
Difix3D+ [40]	14.36	15.53	16.16	15.35	0.492	0.538	0.594	0.541	0.404	0.416	0.336	0.385
GenFusion [47]	12.82	16.42	17.83	15.69	0.502	0.609	0.646	0.586	0.541	0.478	0.469	0.496
Ours	17.48	19.87	21.64	19.67	0.639	0.678	0.731	0.683	0.368	0.267	0.233	0.289

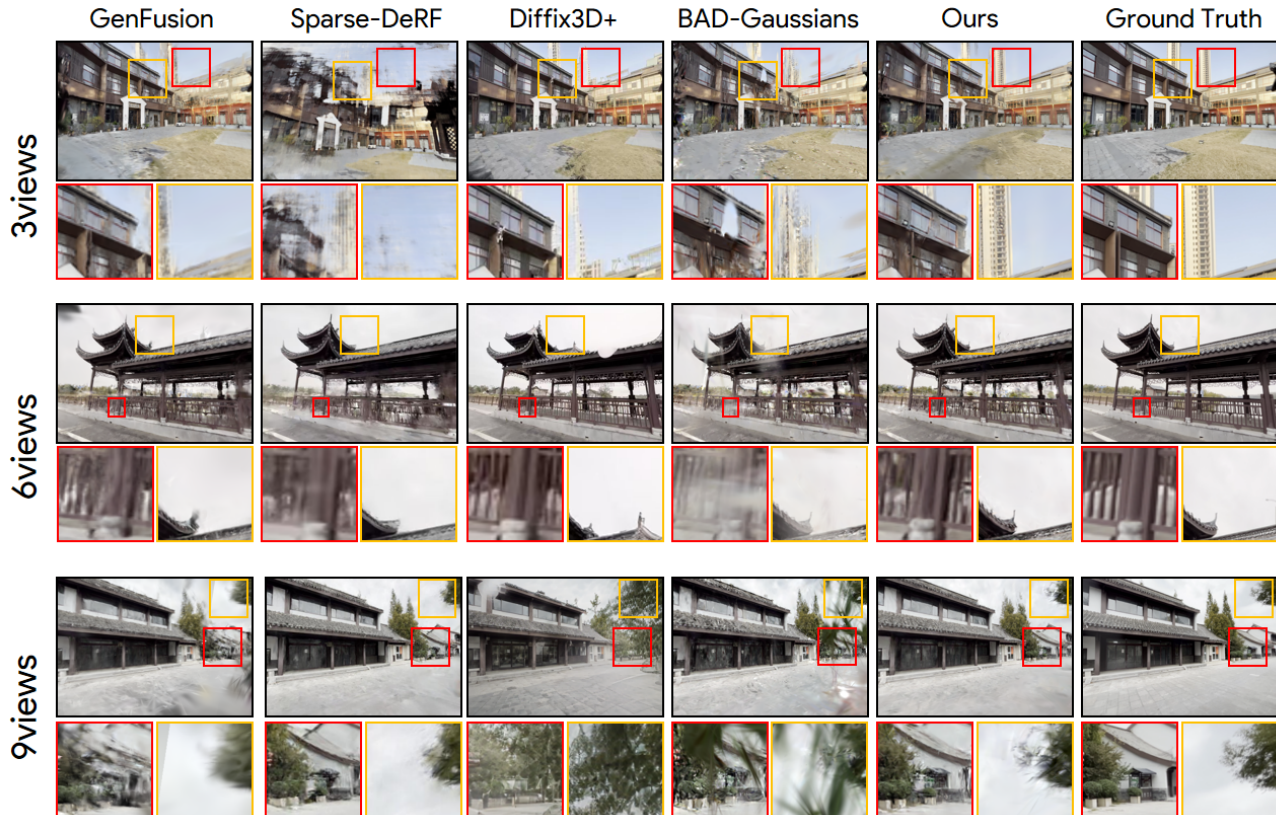


Fig. 6: **Qualitative results of novel view synthesis on proposed DL3DV-BLUR Dataset.** Compared the novel view with other methods with baselines rendering quality using 3, 6, and 9 input views, our approach produces more realistic rendering results with fine-grained details.

of our approach in handling the ill-posed problem of sparse deblurring, where traditional constraints typically collapse.

Qualitative results provided in Fig. 5 highlight the superior fidelity and structural coherence of CoherentGS. While our method reconstructs photorealistic textures with sharp edges, competing approaches suffer from distinct failure modes inherent to their paradigms. Specifically, Sparse-DeRF struggles to resolve fine-grained geometry due to the ambiguity caused by sparse, motion-blurred inputs. More critically, while diffusion-guided methods like Difix3D+ and GenFusion employ strong generative priors to enhance visual quality, they rely heavily on fixed camera poses estimated from degraded observations. This dependency creates a critical bottleneck: when initial trajectories are inaccurate, the resulting projection

misalignments are erroneously baked into the geometry by the generative prior, causing structural distortions rather than correcting them. Furthermore, the severe blur corrupts the semantic evidence required by these priors, making diffusion models prone to hallucinating content that contradicts the underlying scene. By jointly refining camera poses and scene representation, CoherentGS breaks this error propagation loop, yielding results that are not only visually pleasing but also geometrically faithful to the true scene.

Evaluation of Generalization in large-scale scenes. To evaluate the robustness of CoherentGS in unstructured environments, we use the proposed DL3DV-Blur which is simulated motion blur on five outdoor scenes and conduct assessments under sparse-input protocols (3, 6, and 9 views). As reported

TABLE III: Quantitative comparison of novel view synthesis on the real-scene dataset [2]. We compare the rendering quality with baselines given 3, 6, and 9 views. Each column is colored as: **best** and **second best**.

Method	PSNR \uparrow				SSIM \uparrow				LPIPS \downarrow			
	3-view	6-view	9-view	Average	3-view	6-view	9-view	Average	3-view	6-view	9-view	Average
BAD-Gaussians [22]	18.57	20.61	21.99	20.39	0.495	0.619	0.659	0.591	0.337	0.257	0.216	0.270
Sparse-DeRF* [39]	17.78	20.01	21.16	19.65	0.463	0.598	0.618	0.560	0.379	0.281	0.242	0.300
Difix3D+ [40]	18.06	19.50	19.79	19.12	0.533	0.574	0.585	0.564	0.415	0.390	0.368	0.391
GenFusion [47]	13.42	15.95	16.19	15.18	0.346	0.473	0.472	0.430	0.588	0.533	0.540	0.554
Ours	19.57	22.01	23.44	21.67	0.575	0.681	0.747	0.668	0.297	0.201	0.167	0.221

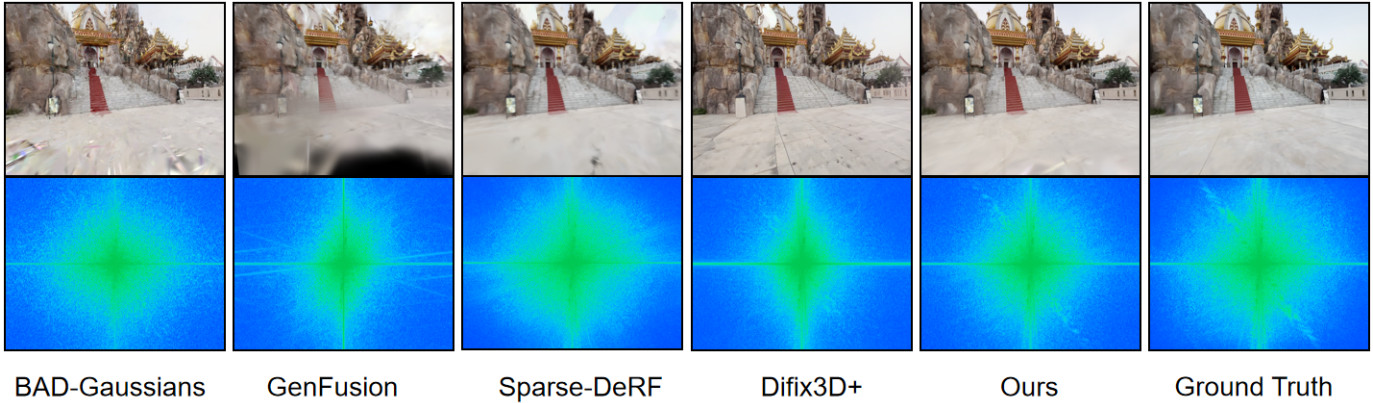


Fig. 7: **Frequency Spectrum Analysis.** Compared to BAD-Gaussians and GenFusion, our approach produces a frequency distribution that closely aligns with the *Ground Truth*. This confirms that our method effectively recovers realistic textures while suppressing the directional artifacts common in generative priors.

TABLE IV: Ablation study of our method’s components.

CoherentGS	PSNR \uparrow	SSIM \uparrow	LPIPS \downarrow
baseline	19.58	0.555	0.274
+Geometric Priors	20.59	0.615	0.218
+Deblurring Priors	20.83	0.647	0.207
+Depth Loss	21.12	0.671	0.195

in Table I, CoherentGS consistently outperforms competing methods across all sparsity levels, demonstrating strong generalization capabilities in geometrically complex, unseen scenarios. Beyond numerical improvements, our method delivers superior visual fidelity. In contrast to generative 3DGS-based baselines like Difix3D+ and GenFusion, which tend to over-smooth fine details, CoherentGS effectively preserves high-frequency textures and intricate geometric structures. This results in sharper object boundaries and a more faithful reconstruction of thin or cluttered elements. Qualitative results in Fig. 6 further highlight these advantages, confirming that CoherentGS produces geometrically clear and view-consistent renderings, even when optimized from sparsely sampled and severely blurred observations.

Spectral Analysis via Fast Fourier Transform. To validate structural fidelity beyond the spatial domain, we compare the spectra of BAD-Gaussians, GenFusion, Sparse-DeRF, Difix3D+ and our synthesized views against the Ground Truth (GT) using 2D Fast Fourier Transform (FFT). As shown in Fig. 7, the GT spectrum exhibits a compact low-frequency center

that decays naturally into rich, slightly asymmetrical high-frequency structures, reflecting the scene’s diverse and natural geometric details. Our method produces a spectral profile highly congruent with the GT, preserving the scale of central energy concentration and the irregular high-frequency distribution with minimal amplitude loss. This indicates that CoherentGS effectively suppresses blur while recovering realistic textures without introducing structural artifacts. In contrast, the spectrum of BAD-Gaussians displays a rapid radial energy decay, indicating a severe attenuation of high-frequency components. This confirms that the optimization process over-smooths the reconstruction, failing to recover fine edges and details. Conversely, GenFusion and Difix3D+ manifests prominent horizontal and vertical spectral spikes and distinct sidelobes. This anisotropic energy concentration corresponds to directional grid-like artifacts rather than naturally distributed textures. Although GenFusion exhibits strong high-frequency amplitude, its deviation from the GT pattern implies that the generated details are largely spectral hallucinations or structural noise. Overall, our method achieves the closest frequency-domain alignment with GT, corroborating that our diffusion-guided prior maintains semantic and structural fidelity while avoiding both over-smoothing and artifact induction.

Efficiency Analysis of Training and Inference. To verify the computational efficiency of the proposed method, we compare the Storage consumption as well as the training and inference

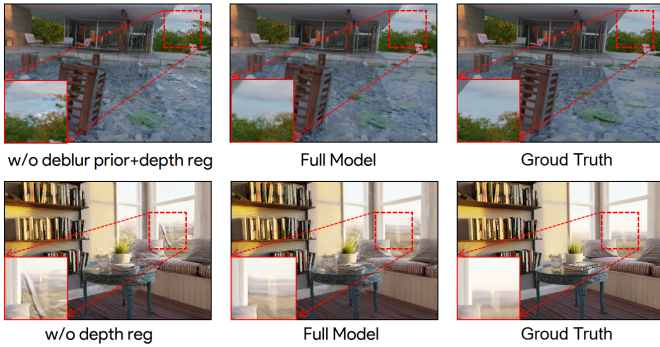


Fig. 8: **Visual ablation of the Supervised Signals.** We compare our model against variants lacking specific components to validate their contributions.

time of different approaches on the DL3DV-Blur dataset. As shown in Table V, under a unified setting, the number of training iterations for Gaussian-based methods is fixed to 7000 steps, while Sparse-DeRF is trained for 200000 steps. After training, we perform a single rendering of a video sequence with 30 fps and 240 frames in total. Compared with Bad-Gaussians, which relies solely on photometric reprojection, our CoherentGS even after introducing a diffusion prior and a deblur prior as additional supervision, only increases storage consumption to 16.8G, and the training time rises by merely 3.1 min. The inference time is 0.6 min, accounting for less than 5% of the overall runtime. This indicates that the extra computational cost remains modest while achieving significantly improved reconstruction quality. Compared with Difx3D+ and GenFusion, which depend on complex inference pipelines, CoherentGS further demonstrates an advantage in overall efficiency. By explicitly integrating priors during training, CoherentGS substantially simplifies the inference procedure. In contrast to Sparse-DeRF, which requires 25.6G memory and up to 132h of training, CoherentGS is one order of magnitude more efficient in terms of both memory and time, while still delivering high-quality reconstructions and being more friendly to practical computational budgets.

Method	Storage	Training Time	Inference Time
(a) Bad-Gaussians	9.63G	8.6min	0.5min
(b) Difx3D+	14.9G	3.7min	6.9min
(c) Genfusion	20.2G	3.9min	9.19min
(d) Sparse-DeRF	25.6G	132h	1.8min
(e) Ours	16.8G	11.7min	0.6min

TABLE V: Comparison of GPU storage usage, training time, and inference time of different methods on the DL3DV-Blur dataset. CoherentGS maintains competitive storage and training cost while significantly reducing inference overhead.

C. Ablation Study

Effectiveness of Supervised Signals. To dissect the contribution of each component, we conduct an ablation study on the synthetic dataset under the 3-view setting, sequentially incorporating the diffusion prior, deblur prior, and depth regularization. We take Bad-gaussians as our baseline. Quantitative

TABLE VI: Ablation study on different camera trajectories.

Trajectory	PSNR \uparrow	SSIM \uparrow	LPIPS \downarrow
Linear interpolation	17.24	0.575	0.372
Ellipse sampling	15.64	0.550	0.428
SACN	17.48	0.639	0.368

results in Table IV show that our full model consistently yields the best performance across all metrics. The qualitative comparisons in Fig. 8 further reveal the underlying mechanics of these components. Specifically, removing the deblur prior significantly degrades 3D consistency. Under sparse and blurry conditions, the geometry is inherently ambiguous. Without the deblur prior acting as a semantic anchor, the diffusion model struggles to distinguish between high-frequency textures and blur artifacts, leading to inconsistent hallucinations across views. By explicitly decoupling texture from motion blur, the deblur prior provides a cleaner guidance signal for generative refinement. Complementing this, depth regularization proves essential for suppressing geometric noise. Omitting this term results in severe floating artifacts and near-camera noise in novel views. A critical insight here is that since the diffusion prior primarily optimizes 2D appearance, it may satisfy visual constraints by projecting realistic textures onto erroneous geometry (e.g., floaters). The depth regularization enforces geometric smoothness, ensuring that the perceptual improvements translate into correct underlying 3D structures rather than superficial texture mapping.

Effectiveness of SACN. To validate the effectiveness of our proposed Scene Adaptive Consistency Normalization, we compare it against two standard interpolation strategies: linear interpolation and elliptical trajectory interpolation. As visualized in Fig. 9, standard strategies suffer from inherent limitations: Linear interpolation constrains novel views to the baseline between input frames. This strategy offers minimal information gain, as the rendered views provide limited angular variation and fail to expose occluded or under-optimized regions to the diffusion prior. Consequently, the optimization becomes inefficient due to semantic redundancies. Conversely, elliptical interpolation maximizes angular coverage but often ventures into unobserved regions outside the visual hull of the input views. Since the diffusion prior lacks contextual image evidence in these blind spots, it tends to hallucinate content that is inconsistent with the true scene. Forcing the model to incorporate these erroneous priors will lead to artifact propagation and geometric distortion.

In contrast, our strategy achieves reliability-aware exploration. It actively guides the camera to explore regions that are geometrically uncertain yet semantically recoverable. By maximizing the potential of the diffusion prior within a reliable trust region, our method effectively repairs artifacts while avoiding the semantic inconsistencies caused by aggressive sampling. Quantitative results in Table VI confirm that this reference-guided strategy significantly improves reconstruction quality compared to topology-agnostic sampling methods.

Analysis of Warm-up Strategy. To determine the optimal

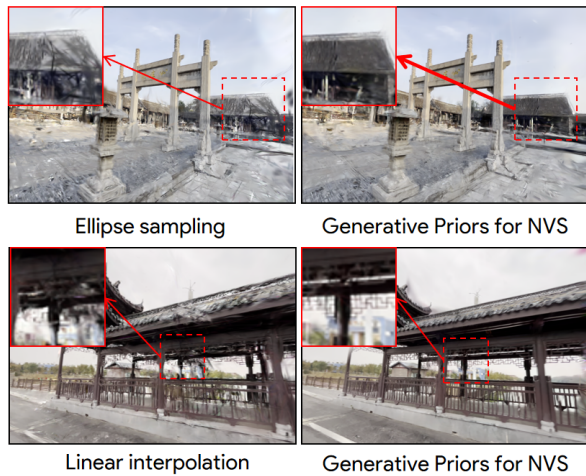


Fig. 9: **Effectiveness of the SACN Strategy.** We compare with widely used linear interpolation and ellipse sampling. The red boxes show the most prominent differences.

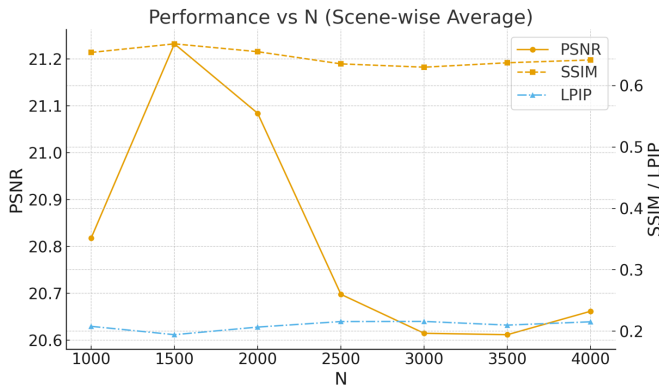


Fig. 10: **Analysis of the Warm-up Strategy.** The model achieves the best balance between geometric stability and semantic refinement at $N = 1500$, yielding the highest scores.

timing for introducing the generative prior, we evaluate performance across different warm-up iterations. As shown in Fig. 10, the reconstruction quality exhibits a clear unimodal trend. Premature Injection: Introducing the diffusion prior too early (e.g., before the deblurring module converges) is detrimental. At this stage, the scene representation has not yet disentangled motion blur from geometry. Consequently, the generative prior risks interpreting motion blur as intrinsic texture, erroneously solidifying low-frequency artifacts into the model. Delayed Injection: Conversely, introducing the prior too late leaves an insufficient optimization window. With limited iterations remaining, the gradient guidance from the diffusion prior fails to fully propagate to unseen regions, resulting in sub-optimal refinement and limiting the quality of synthesized views. Our empirical results suggest that waiting for the explicit deblurring module to stabilize before injecting the prior achieves the best balance.

VI. CONCLUSION AND LIMITATIONS

Conclusion. In this paper, we present CoherentGS, a novel 3D Gaussian Splatting framework designed to achieve high-fidelity 3D reconstruction from sparse and motion-blurred inputs. We identify that these prevalent real-world degradations create a vicious cycle where sparse views impede blur resolution, and blur degrades high-frequency details essential for view alignment, leading to fragmented reconstructions and low-frequency bias. To effectively break this cycle, our core contribution is a synergistic dual-prior strategy. This strategy intelligently integrates a specialized deblurring network for robust photometric guidance and a powerful diffusion model providing geometric priors for scene completion. These are further supported by a consistency-guided camera exploration module for adaptive viewpoint planning and a depth regularization loss for geometric plausibility. Extensive quantitative and qualitative experiments on both synthetic and real-world scenes, utilizing as few as 3, 6, and 9 input views, unequivocally demonstrate CoherentGS’s superior performance. Our method consistently outperforms existing state-of-the-art approaches, delivering significantly more coherent, detailed, and visually realistic novel view syntheses under challenging conditions. CoherentGS thus establishes a new benchmark for robust 3D reconstruction from degraded inputs, substantially expanding the practical applicability of 3DGS.

Limitations. While our proposed CoherentGS significantly advances 3D reconstruction from sparse and motion-blurred inputs, its current design focuses primarily on these specific degradations. Our framework is not yet optimized to robustly handle other common real-world challenges, such as defocus blur, overexposed or dark images, and complex degraded effects. Addressing these additional types of degraded inputs, potentially through the integration of more generalized priors or multi-degradation modeling, presents a promising avenue for future work to further broaden CoherentGS’s applicability in diverse and challenging scenarios.

REFERENCES

- [1] B. Kerbl, G. Kopanas, T. Leimkühler, and G. Drettakis, “3d gaussian splatting for real-time radiance field rendering,” *ACM Transactions on Graphics (TOG)*, 2023. [Online]. Available: <https://repo-sam.inria.fr/fungraph/3d-gaussian-splatting/>
- [2] L. Ma, X. Li, J. Liao, Q. Zhang, X. Wang, J. Wang, and P. V. Sander, “Deblur-NeRF: Neural Radiance Fields from Blurry Images,” in *Computer Vision and Pattern Recognition (CVPR)*, 2022. [Online]. Available: <https://limacv.github.io/deblurner/>
- [3] J. Oh, J. Chung, D. Lee, and K. M. Lee, “DeblurGS: Gaussian splatting for camera motion blur,” *arXiv preprint arXiv:2404.11358*, 2024.
- [4] H. Li, H. Cao, B. Feng, Y. Shao, X. Tang, Z. Yan, L. Yuan, Y. Tian, and Y. Li, “Beyond chemical qa: Evaluating llm’s chemical reasoning with modular chemical operations,” *arXiv preprint arXiv:2505.21318*, 2025.
- [5] W. Chen and L. Liu, “Deblur-gs: 3d gaussian splatting from camera motion blurred images,” *Proceedings of the ACM on Computer Graphics and Interactive Techniques*, vol. 7, no. 1, pp. 1–15, 2024.
- [6] B. Lee, H. Lee, X. Sun, U. Ali, and E. Park, “Deblurring 3d gaussian splatting,” in *European Conference on Computer Vision*. Springer, 2024, pp. 127–143.
- [7] T. Lu, M. Yu, L. Xu, Y. Xiangli, L. Wang, D. Lin, and B. Dai, “Scaffold-gs: Structured 3d gaussians for view-adaptive rendering,” in *Proceedings of the IEEE/CVF Conference on Computer Vision and Pattern Recognition*, 2024, pp. 20 654–20 664.

- [8] Z. Tang, J. Zhang, X. Cheng, W. Yu, C. Feng, Y. Pang, B. Lin, and L. Yuan, "Cycle3d: High-quality and consistent image-to-3d generation via generation-reconstruction cycle," *arXiv preprint arXiv:2407.19548*, 2024.
- [9] H. Li, D. Long, L. Yuan, Y. Wang, Y. Tian, X. Wang, and F. Mo, "Decoupled peak property learning for efficient and interpretable electronic circular dichroism spectrum prediction," *Nature Computational Science*, vol. 5, no. 3, pp. 234–244, 2025.
- [10] J. Wang, Y. Ma, J. Guo, Y. Xiao, G. Huang, and X. Li, "Cove: Unleashing the diffusion feature correspondence for consistent video editing," *arXiv preprint arXiv:2406.08850*, 2024.
- [11] Z. Fan, W. Cong, K. Wen, K. Wang, J. Zhang, X. Ding, D. Xu, B. Ivanovic, M. Pavone, G. Pavlakos, Z. Wang, and Y. Wang, "Instantsplat: Unbounded sparse-view pose-free gaussian splatting in 40 seconds," 2024.
- [12] K. Feng, Y. Ma, B. Wang, C. Qi, H. Chen, Q. Chen, and Z. Wang, "Dit4edit: Diffusion transformer for image editing," *arXiv preprint arXiv:2411.03286*, 2024.
- [13] J. Zhang, Z. Tang, Y. Pang, X. Cheng, P. Jin, Y. Wei, W. Yu, M. Ning, and L. Yuan, "Repaint123: Fast and high-quality one image to 3d generation with progressive controllable 2d repainting," *arXiv preprint arXiv:2312.13271*, 2023.
- [14] Y. Bao, T. Ding, J. Huo, Y. Liu, Y. Li, W. Li, Y. Gao, and J. Luo, "3d gaussian splatting: Survey, technologies, challenges, and opportunities," *IEEE Transactions on Circuits and Systems for Video Technology*, 2025.
- [15] Y. Zhao, R. Ye, R. Zheng, Z. Cheng, C. Feng, J. Yang, P. Qiao, C. Liu, and J. Chen, "Tune-your-style: Intensity-tunable 3d style transfer with gaussian splatting," in *Proceedings of the IEEE/CVF International Conference on Computer Vision*, 2025, pp. 19 032–19 042.
- [16] C. Cheng, Y. Hu, S. Yu, B. Zhao, Z. Wang, and H. Wang, "Reggs: Unposed sparse views gaussian splatting with 3dgs registration," *arXiv preprint arXiv:2507.08136*, 2025.
- [17] Z. Liu, J. Su, G. Cai, Y. Chen, B. Zeng, and Z. Wang, "Georgs: Geometric regularization for real-time novel view synthesis from sparse inputs," *IEEE Transactions on Circuits and Systems for Video Technology*, 2024.
- [18] W. Yu, C. Feng, J. Tang, X. Jia, L. Yuan, and Y. Tian, "Evagaussians: Event stream assisted gaussian splatting from blurry images," *arXiv preprint arXiv:2405.20224*, 2024.
- [19] X. Lin, S. Luo, X. Shan, X. Zhou, C. Ren, L. Qi, M.-H. Yang, and N. Vasconcelos, "Hggs: High-quality novel view synthesis with gaussian splatting in degraded scenes," in *The Thirteenth International Conference on Learning Representations*.
- [20] J. Zhang, F. Zhan, M. Xu, S. Lu, and E. Xing, "Fregs: 3d gaussian splatting with progressive frequency regularization," in *Proceedings of the IEEE/CVF Conference on Computer Vision and Pattern Recognition*, 2024, pp. 21 424–21 433.
- [21] Z. Tang, C. Feng, X. Cheng, W. Yu, J. Zhang, Y. Liu, X. Long, W. Wang, and L. Yuan, "Neuralgs: Bridging neural fields and 3d gaussian splatting for compact 3d representations," *arXiv preprint arXiv:2503.23162*, 2025.
- [22] L. Zhao, P. Wang, and P. Liu, "Bad-gaussians: Bundle adjusted deblur gaussian splatting," *arXiv preprint arXiv:2403.11831*, 2024.
- [23] S. Dai and Y. Wu, "Motion from blur," in *2008 IEEE conference on computer vision and pattern recognition*. IEEE, 2008, pp. 1–8.
- [24] H. Son, J. Lee, S. Cho, and S. Lee, "Real-time video deblurring via lightweight motion compensation," in *Computer Graphics Forum*, vol. 41, no. 7. Wiley Online Library, 2022, pp. 177–188.
- [25] K. Nie, X. Shi, S. Cheng, Z. Gao, and J. Xu, "High frame rate video reconstruction and deblurring based on dynamic and active pixel vision image sensor," *IEEE Transactions on Circuits and Systems for Video Technology*, vol. 31, no. 8, pp. 2938–2952, 2020.
- [26] P. Wang, L. Zhao, R. Ma, and P. Liu, "BAD-NeRF: Bundle Adjusted Deblur Neural Radiance Fields," in *Computer Vision and Pattern Recognition (CVPR)*, 2023. [Online]. Available: <https://wangpeng000.github.io/BAD-NeRF/>
- [27] L. Ma, X. Li, J. Liao, Q. Zhang, X. Wang, J. Wang, and P. V. Sander, "Deblur-nerf: Neural radiance fields from blurry images," in *Proceedings of the IEEE/CVF Conference on Computer Vision and Pattern Recognition*, 2022, pp. 12 861–12 870.
- [28] B. Mildenhall, P. P. Srinivasan, M. Tancik, J. T. Barron, R. Ramamoorthi, and R. Ng, "NeRF: Representing Scenes as Neural Radiance Fields for View Synthesis," in *European Conference on Computer Vision (ECCV)*, 2020. [Online]. Available: <https://www.matthewtancik.com/nerf>
- [29] D. Lee, M. Lee, C. Shin, and S. Lee, "Dp-nerf: Deblurred neural radiance field with physical scene priors," in *Computer Vision and Pattern Recognition (CVPR)*, 2023.
- [30] D. Lee, J. Oh, J. Rim, S. Cho, and K. M. Lee, "Exblurf: Efficient radiance fields for extreme motion blurred images," in *Proceedings of the IEEE/CVF International Conference on Computer Vision*, 2023, pp. 17 639–17 648.
- [31] C. Peng and R. Chellappa, "Pdrf: progressively deblurring radiance field for fast scene reconstruction from blurry images," in *Proceedings of the AAAI Conference on Artificial Intelligence*, vol. 37, no. 2, 2023, pp. 2029–2037.
- [32] C. Feng, W. Yu, X. Cheng, Z. Tang, J. Zhang, L. Yuan, and Y. Tian, "Ae-nerf: Augmenting event-based neural radiance fields for non-ideal conditions and larger scenes," in *Proceedings of the AAAI Conference on Artificial Intelligence*, vol. 39, no. 3, 2025, pp. 2924–2932.
- [33] W. Chen and L. Liu, "Deblur-gs: 3d gaussian splatting from camera motion blurred images," *Proceedings of the ACM on Computer Graphics and Interactive Techniques*, vol. 7, no. 1, pp. 1–15, 2024.
- [34] B. Lee, H. Lee, X. Sun, U. Ali, and E. Park, "Deblurring 3d gaussian splatting," in *European Conference on Computer Vision*. Springer, 2024, pp. 127–143.
- [35] Y. Lu, Y. Zhou, D. Liu, T. Liang, and Y. Yin, "Bard-gs: Blur-aware reconstruction of dynamic scenes via gaussian splatting," in *Proceedings of the Computer Vision and Pattern Recognition Conference*, 2025, pp. 16 532–16 542.
- [36] M.-Q. V. Bui, J. Park, J. L. G. Bello, J. Moon, J. Oh, and M. Kim, "Mobgs: Motion deblurring dynamic 3d gaussian splatting for blurry monocular video," *arXiv preprint arXiv:2504.15122*, 2025.
- [37] C. Feng, Z. Tang, W. Yu, Y. Pang, Y. Zhao, J. Zhao, L. Yuan, and Y. Tian, "E-4dgs: High-fidelity dynamic reconstruction from the multi-view event cameras," in *Proceedings of the 33rd ACM International Conference on Multimedia*, 2025, pp. 7356–7365.
- [38] R. Wu, Z. Zhang, M. Chen, X. Fan, Z. Yan, and W. Zuo, "Deblur4dgs: 4d gaussian splatting from blurry monocular video," *arXiv preprint arXiv:2412.06424*, 2024.
- [39] D. Lee, D. Kim, J. Lee, M. Lee, S. Lee, and S. Lee, "Sparse-derf: Deblurred neural radiance fields from sparse view," *IEEE Transactions on Pattern Analysis and Machine Intelligence*, vol. 47, no. 8, pp. 6842–6858, 2025.
- [40] J. Z. Wu, Y. Zhang, H. Turki, X. Ren, J. Gao, M. Z. Shou, S. Fidler, Z. Gojcic, and H. Ling, "Difix3d+: Improving 3d reconstructions with single-step diffusion models," in *Proceedings of the Computer Vision and Pattern Recognition Conference*, 2025, pp. 26 024–26 035.
- [41] X. Yin, Q. Zhang, Y. Chang, Y. Feng, Q. Fan, X. Yang, C.-M. Pun, H. Zhang, and X. Cun, "Gsfixer: Improving 3d gaussian splatting with reference-guided video diffusion priors," *arXiv preprint arXiv:2508.09667*, 2025.
- [42] Y. Luo, S. Zhou, Y. Lan, X. Pan, and C. C. Loy, "3denhancer: Consistent multi-view diffusion for 3d enhancement," in *Proceedings of the Computer Vision and Pattern Recognition Conference*, 2025, pp. 16 430–16 440.
- [43] Y. Zhong, Z. Li, D. Z. Chen, L. Hong, and D. Xu, "Taming video diffusion prior with scene-grounding guidance for 3d gaussian splatting from sparse inputs," in *Proceedings of the Computer Vision and Pattern Recognition Conference*, 2025, pp. 6133–6143.
- [44] W. Yu, J. Xing, L. Yuan, W. Hu, X. Li, Z. Huang, X. Gao, T.-T. Wong, Y. Shan, and Y. Tian, "Viewcrafter: Taming video diffusion models for high-fidelity novel view synthesis," *arXiv preprint arXiv:2409.02048*, 2024.
- [45] F. Liu, W. Sun, H. Wang, Y. Wang, H. Sun, J. Ye, J. Zhang, and Y. Duan, "Reconx: Reconstruct any scene from sparse views with video diffusion model," *arXiv preprint arXiv:2408.16767*, 2024.
- [46] R. Wu, B. Mildenhall, P. Henzler, K. Park, R. Gao, D. Watson, P. P. Srinivasan, D. Verbin, J. T. Barron, B. Poole *et al.*, "Reconfusion: 3d reconstruction with diffusion priors," in *Proceedings of the IEEE/CVF conference on computer vision and pattern recognition*, 2024, pp. 21 551–21 561.
- [47] S. Wu, C. Xu, B. Huang, A. Geiger, and A. Chen, "Genfusion: Closing the loop between reconstruction and generation via videos," in *Proceedings of the Computer Vision and Pattern Recognition Conference*, 2025, pp. 6078–6088.
- [48] A. Paliwal, X. Zhou, W. Ye, J. Xiong, R. Ranjan, and N. K. Kalantari, "Ri3d: Few-shot gaussian splatting with repair and inpainting diffusion priors," *arXiv preprint arXiv:2503.10860*, 2025.
- [49] J. Wei, S. Leutenegger, and S. Schaefer, "Gsfix3d: Diffusion-guided repair of novel views in gaussian splatting," *arXiv preprint arXiv:2508.14717*, 2025.
- [50] E. Weber, A. Holynski, V. Jampani, S. Saxena, N. Snavely, A. Kar, and A. Kanazawa, "Nerfiller: Completing scenes via generative 3d inpainting," in *Proceedings of the IEEE/CVF Conference on Computer Vision and Pattern Recognition*, 2024, pp. 20 731–20 741.

- [51] Y. Li, X. Wang, J. Wu, Y. Ma, and Z. Jin, "Sparsegs-w: Sparse-view 3d gaussian splatting in the wild with generative priors," *arXiv preprint arXiv:2503.19452*, 2025.
- [52] M. YU, W. Hu, J. Xing, and Y. Shan, "Trajectorycrafter: Redirecting camera trajectory for monocular videos via diffusion models," *arXiv preprint arXiv:2503.05638*, 2025.
- [53] Y. Zhang and D. Yan, "Knowledge distillation for image restoration: Simultaneous learning from degraded and clean images," in *ICASSP 2025-2025 IEEE International Conference on Acoustics, Speech and Signal Processing (ICASSP)*. IEEE, 2025, pp. 1–5.
- [54] J. L. Schonberger and J.-M. Frahm, "Structure-from-motion Revisited," in *Computer Vision and Pattern Recognition (CVPR)*, 2016. [Online]. Available: <https://github.com/colmap/colmap>
- [55] J. C. Lee, D. Rho, X. Sun, J. H. Ko, and E. Park, "Compact 3d gaussian representation for radiance field," in *Proceedings of the IEEE/CVF Conference on Computer Vision and Pattern Recognition*, 2024, pp. 21 719–21 728.
- [56] S. W. Zamir, A. Arora, S. Khan, M. Hayat, F. S. Khan, M.-H. Yang, and L. Shao, "Multi-stage progressive image restoration," in *Proceedings of the IEEE/CVF conference on computer vision and pattern recognition*, 2021, pp. 14 821–14 831.
- [57] K. Simonyan and A. Zisserman, "Very deep convolutional networks for large-scale image recognition," *arXiv preprint arXiv:1409.1556*, 2014.
- [58] B. Poole, A. Jain, J. T. Barron, and B. Mildenhall, "Dreamfusion: Text-to-3d using 2d diffusion," *arXiv preprint arXiv:2209.14988*, 2022.
- [59] M. Niemeyer, J. T. Barron, B. Mildenhall, M. S. Sajjadi, A. Geiger, and N. Radwan, "RegNeRF: Regularizing Neural Radiance Fields for View Synthesis from Sparse Inputs," in *Computer Vision and Pattern Recognition (CVPR)*, 2022. [Online]. Available: <https://m-niemeyer.github.io/regnerf/>
- [60] L. Ling, Y. Sheng, Z. Tu, W. Zhao, C. Xin, K. Wan, L. Yu, Q. Guo, Z. Yu, Y. Lu *et al.*, "Dl3dv-10k: A large-scale scene dataset for deep learning-based 3d vision," in *Proceedings of the IEEE/CVF Conference on Computer Vision and Pattern Recognition*, 2024, pp. 22 160–22 169.
- [61] R. Zhang, P. Isola, A. A. Efros, E. Shechtman, and O. Wang, "The unreasonable effectiveness of deep features as a perceptual metric," in *Proceedings of the IEEE conference on computer vision and pattern recognition*, 2018, pp. 586–595.
- [62] S. Zhou, J. Zhang, W. Zuo, H. Xie, J. Pan, and J. S. Ren, "Davanet: Stereo deblurring with view aggregation," in *Proceedings of the IEEE/CVF Conference on Computer Vision and Pattern Recognition*, 2019, pp. 10 996–11 005.
- [63] S. Niklaus, L. Mai, and F. Liu, "Video frame interpolation via adaptive separable convolution," in *IEEE International Conference on Computer Vision*, 2017.
- [64] L. Kong, J. Dong, J. Tang, M.-H. Yang, and J. Pan, "Efficient visual state space model for image deblurring," in *CVPR*, 2025.
- [65] A. Sauer, D. Lorenz, A. Blattmann, and R. Rombach, "Adversarial diffusion distillation," in *European Conference on Computer Vision*. Springer, 2025, pp. 87–103.

A. Dataset Details

DL3DV-BLUR Dataset. To rigorously assess the generalization capability of CoherentGS in complex, unconstrained outdoor environments, we establish a new benchmark named DL3DV-BLUR, derived from five diverse scenes within the DL3DV-10K dataset [60]. In constructing this dataset, we strictly adhere to the *high-fidelity blur generation protocol* proposed in DAVANet [62]. As analyzed in [62], synthesizing motion blur by simply averaging frames from low-fps video sequences is insufficient to approximate realistic long-exposure photography. Such low-temporal-resolution accumulation inevitably introduces discontinuous ghosting artifacts and temporal aliasing, which differ significantly from the continuous integral of light on a camera sensor.

To address this and simulate physically realistic blur, we adopt the following pipeline:

- 1) **Preprocessing for Diffusion Alignment:** First, to ensure compatibility with the spatial alignment requirements of the latent diffusion model, we resize the original video resolution from 960×540 to 960×536 .
- 2) **High-Frame-Rate Interpolation:** Following the strategy in [62], we employ the high-quality frame interpolation method SepConv-Slomo [63] to temporally upsample the source footage to 480 fps. This dense temporal sampling is crucial for filling the gaps between frames, thereby suppressing discrete artifacts.
- 3) **Blur Generation via Accumulation:** We generate the final motion-blurred images by mathematically approximating the exposure integration process. This is achieved by averaging a sliding window of varying sizes (specifically 6 and 10 frames from the interpolated sequence) centered on the corresponding sharp ground truth frame.

This rigorous process ensures that DL3DV-BLUR exhibits smooth, and realistic motion trails, providing a challenging and reliable benchmark for evaluating sparse-view deblurring performance. The dataset is available at [huggingface](#).

DEBLUR-NeRF Dataset. To comprehensively evaluate our method, we conduct experiments on the standard DEBLUR-NeRF benchmark [2], which comprises both synthetic and real-world subsets tailored for varying degrees of motion blur.

- **Synthetic Scenes:** This subset includes five diverse 3D scenes: *Cozyroom*, *Factory*, *Pool*, *Tanabata*, and *Trophy*. These scenes are rendered using Blender, where photorealistic motion blur is physically simulated by accumulating multiple sub-frames along a continuous camera trajectory during the exposure interval. This process ensures that the synthesized blur strictly adheres to the physical image formation model, providing high-quality blurry inputs paired with corresponding sharp Ground Truth for quantitative evaluation.
- **Real-world Scenes:** To assess generalization in unconstrained environments, the dataset provides 10 real-world sequences captured with a handheld camera. These sequences feature complex, non-uniform motion blur caused by natural camera shake and varying lighting conditions. Since pixel-aligned ground truth is unavailable for

TABLE VII: Image indices in training settings.

View selection	3views	6views	9views
DL3DV-BLUR	5,15,25	2,5,10,15,17,25	1,2,5,10,15,17,22,25
Deblur-NeRF	5,15,25	2,5,10,15,17,25	1,2,5,10,15,17,22,25

these in-the-wild captures, we utilize them primarily for qualitative analysis to verify the robustness of our method against real-world degradation.

B. Training Details

Our framework is implemented in PyTorch, building upon the official codebase of BAD-Gaussians [22] and integrating the pre-trained prior from Difix3D+ [40].

Optimization. We employ the Adam optimizer for all learnable parameters. The learning rate schedules and densification strategies for 3D Gaussian primitives strictly follow the default configuration in [1], [22]. For the camera trajectory modeling (Eq. (6)), the learning rates for translation and rotation ($T_{\text{start}}, T_{\text{end}}$) are initialized at 5×10^{-3} and exponentially decayed to 5×10^{-5} . Regarding the loss terms, we set the blurry weight and depth regularization weight to $\lambda_1 = 0.8, \lambda_{\text{D-SSIM}} = 0.2, \lambda_{\text{reg}} = 0.1$. The weights for the deblurring (λ_{pr}) and geometric (λ_{geo}) priors are set to 0.01.

Reliability Thresholds. To adapt to different scene distributions, the confidence thresholds for the score model are calibrated per dataset: we set $\{s_{\text{max}}, s_{\text{min}}\}$ to $\{14.5, 4.5\}$ for the outdoor DL3DV-Blur dataset, and $\{8.5, 2.5\}$ for the synthetic Deblur-NeRF dataset.

Training Protocol. The training spans a total of 7,000 iterations. The process initiates with a warm-up phase of 1500 iterations, focusing on stabilizing the deblurring model and camera poses. Subsequently, we activate the generative branch: the Difix prior is queried every 200 iterations to guide the optimization of under-reconstructed regions. All experiments are conducted on a single NVIDIA A6000 with 48GB memory, taking approximately 12.3 minutes per scene.

Training Scene Indices. In our training pipeline, we adopt fixed viewpoint selection settings for both the Deblur-NeRF dataset and our proposed dataset. The specific image indices used to train *CoherentGS* are detailed in Table VII. Notably, the indices for the 3-view and 6-view settings are constructed as subsets of the 9-view configuration.

C. Network Architectures of Pre-trained Priors

To facilitate robust reconstruction under sparse and degraded observations, our framework integrates two specialized pre-trained models. Here, we detail their architectural designs and specific configurations used in our pipeline.

1) *Deblurring Prior: EVSSM:* For the task of recovering sharp semantic cues from motion-blurred inputs, we adopt the Efficient Visual State Space Model (EVSSM) [64] as our deblurring backbone. Unlike traditional CNN-based methods, EVSSM leverages the linear complexity of State Space Models (SSMs) to efficiently model long-range dependencies, which is critical for restoring large-scale motion blur patterns.

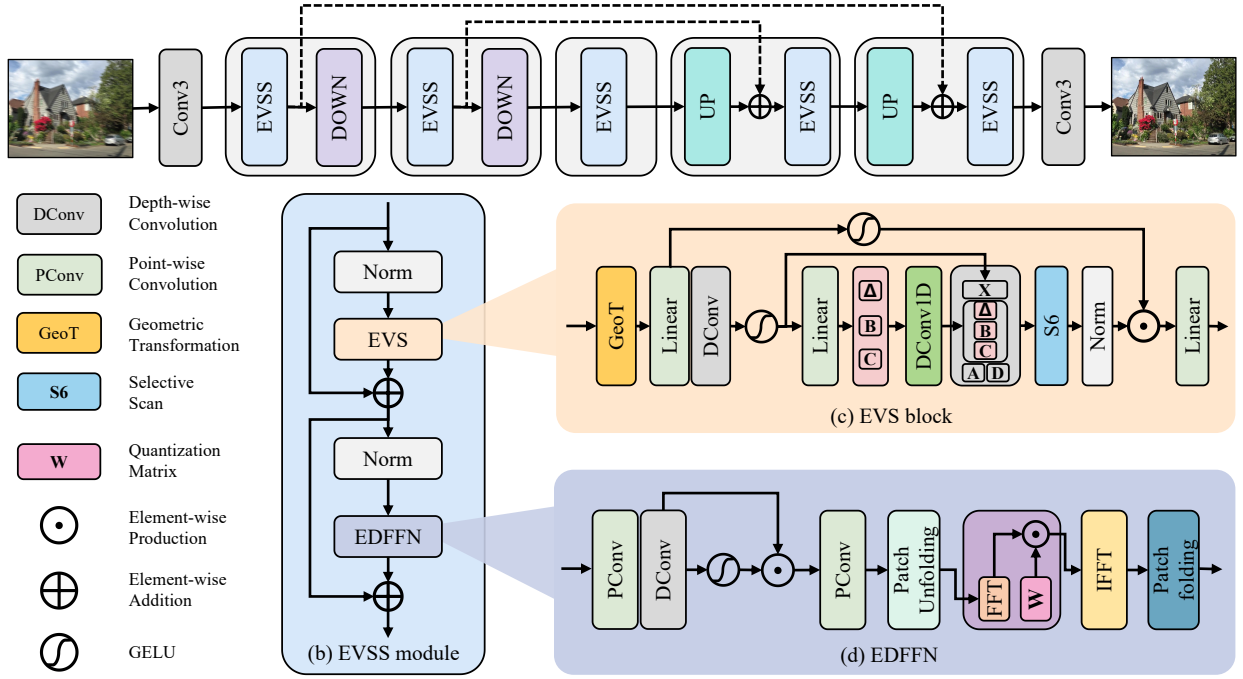


Fig. 11: The pipeline of ESSVM [64].

As shown in Fig.11, the architecture comprises two core components designed to maximize information restoration while minimizing computational overhead:

- **Visual Scanning & Geometric Transformation:** To capture non-local features across different orientations, the input features F_{in} undergo geometric transformations before being processed by SSM core. This multi-directional scanning strategy enhances receptive field without increasing parameter count.
- **Frequency-Aware Filtering:** Recognizing that blur predominantly affects high-frequency components, EVSSM incorporates a Frequency EDFFN module. Features are transformed via Fourier Transform $\mathcal{F}(\cdot)$, allowing the network to explicitly filter and restore spectral components:

$$F_{freq} = \mathcal{F}(F_{in}), \quad F_{out} = \mathcal{Q}(F_{freq}), \quad (19)$$

where $\mathcal{Q}(\cdot)$ denotes the learnable frequency domain filter.

The core temporal modeling is governed by the recursive SSM equations, allowing effective propagation of sharp details:

$$h(t) = \mathbf{A}h(t-1) + \mathbf{B}x(t), \quad y(t) = \mathbf{C}h(t) + \mathbf{D}x(t), \quad (20)$$

where $\mathbf{A}, \mathbf{B}, \mathbf{C}, \mathbf{D}$ are learnable parameters. The final deblurred output is obtained via a residual connection: $I_{deblur} = I_{blur} + \mathcal{R}(I_{blur})$. We utilize the pre-trained weights provided by [64], which have demonstrated superior performance on dynamic scene deblurring.

2) *Generative Prior: Difix:* To rectify geometric artifacts and hallucinate missing textures in sparse-view settings, we employ the DIFIX model from Difix3D+ [40] as our generative prior. Built upon the computationally efficient SD-Turbo [65], DIFIX is specifically fine-tuned to balance artifact removal with structural fidelity. As shown in Fig.12, the key adaptations in DIFIX for 3D-consistent enhancement include:

- **Reference-Conditioned Attention:** To ensure that the generated content remains consistent with the existing 3D scene, DIFIX injects information from clean reference views. This is achieved by concatenating the latent representations of target view \tilde{I} and reference views I_{ref} :

$$z_{joint} = \mathcal{E}(\tilde{I} \oplus I_{ref}) \in \mathbb{R}^{V \times C \times H \times W}, \quad (21)$$

where \mathcal{E} is the encoder and \oplus denotes concatenation. A self-attention mechanism is then applied to z_{joint} to capture cross-view dependencies, enabling the model to borrow sharp details from reference viewpoints.

- **Conservative Noise Level:** Instead of full stochastic generation, DIFIX operates at a reduced noise level ($\tau = 200$). This design choice is crucial for our framework: it allows the model to function as a soft refiner, removing floaters and high-frequency artifacts—without deviating excessively from the original scene layout or introducing uncontrolled hallucinations.

D. Additional Experiment Results

Per-scene Quantitative Breakdown In this section, we provide a comprehensive breakdown of the quantitative evaluation presented in the main manuscript. While the main text reports aggregated metrics averaged across the DEBLUR-NERF and DL3DV-BLUR datasets in Table I, Table II, and Table III, this supplementary section details the scene-wise performance. Table VIII through Table XVI present individual results for each scene under sparse input settings. As evidenced by these detailed comparisons, **CoherentGS** achieves the best quantitative performance in the majority of scenes. It is worth noting that while generative baselines like Difix3D+ occasionally yield competitive scores in specific perceptual metrics, they often suffer from severe view-inconsistency artifacts. Standard

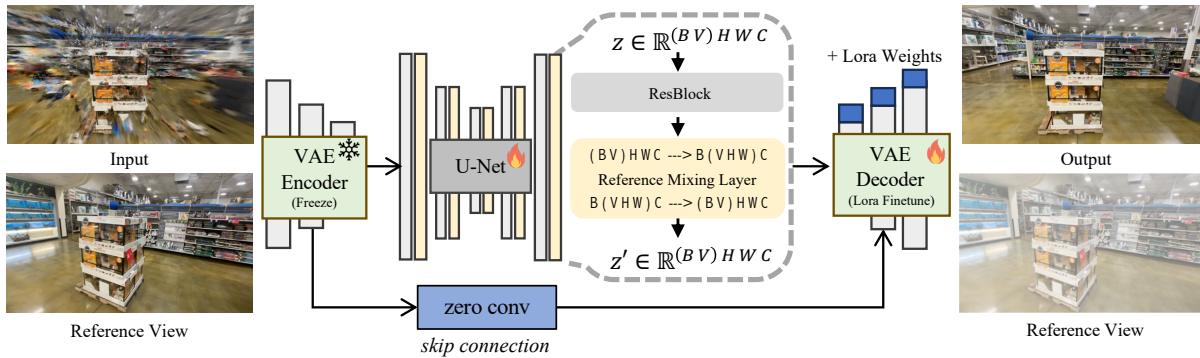


Fig. 12: The pipeline of Difix3D+ [40].

2D metrics of novel view synthesis applied to individual frames may not fully penalize such geometric discrepancies. In contrast, our method maintains superior 3D consistency and structural fidelity while effectively removing motion blur, demonstrating robust performance across diverse scenarios.

scene layout across different views remain consistent with the ground truth, without artifacts. Overall, the results on these three datasets indicate that the deblurring prior significantly improves image sharpness without breaking multi-view geometric consistency.

Geometry Analysis via Rendered Depthmap. To validate the structural consistency of our method, we compare the depth maps of novel views generated by BAD-Gaussians, Difix3D+, and our approach. As shown in Fig. 13, our method produces a more continuous and monotonic depth distribution, with a clear separation between foreground and background, and smooth depth gradients along object surfaces. This indicates that the camera trajectory and 3D geometry are jointly estimated in a more stable manner within a unified framework. In contrast, the depth maps of BAD-Gaussians exhibit globally low contrast, with large regions collapsing to nearly a single depth plane and distant structures being overly smoothed, reflecting that under severe motion blur, relying solely on photometric reprojection leads the geometric solution to degenerate into a low-frequency, blurry structure. Although Difix3D+ is able to preserve part of the foreground contours, its depth maps show pronounced speckle-like noise and discontinuous local fluctuations. This arises from performing de-artifacting independently in the 2D image domain without explicit multi-view geometric consistency constraints, making it difficult for the diffusion model’s per-view textures to remain structurally and geometrically consistent when lifted into 3D space. Overall, this depth comparison further confirms that our diffusion-guided prior effectively maintains global geometric consistency and stability while avoiding both over-smoothing and artifact injection.

Geometric Consistency of the Deblurring Prior Fig. 14 shows the visualization of the deblurring prior on the Deblur-NeRF-Synthetic, Deblur-NeRF-Real, and DL3DV-Blur datasets. For each dataset, the first four images in each row are deblurred views produced by EVSSM, and the last image is the corresponding sharp ground-truth view. We observe that the deblurring prior mainly enhances texture and edge details, while the object contours, occlusion relationships, and overall



Fig. 13: **Depth and Geometry Analysis.** Compared to BAD-Gaussians and Difix3D+, our approach produces reconstructions with significantly improved multi-view geometric consistency, recovering coherent 3D structure while suppressing the directional artifacts commonly introduced by generative priors.

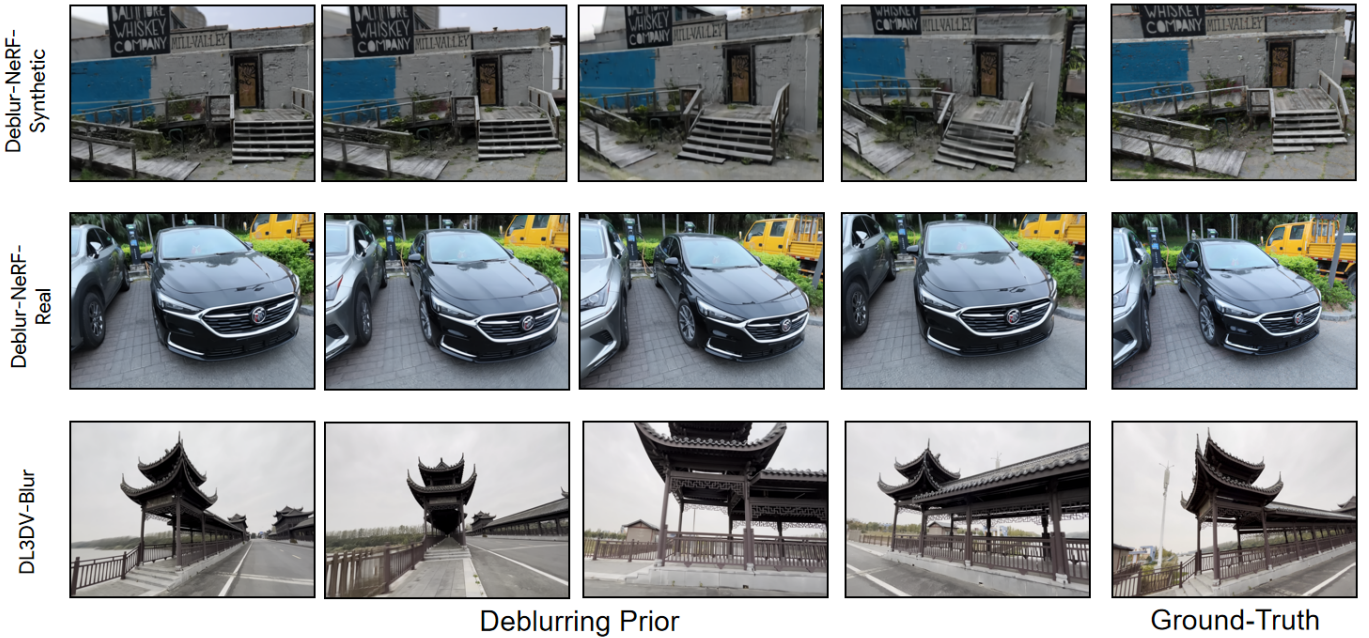


Fig. 14: Visualization of the deblurring prior on Deblur-NeRF-Synthetic, Deblur-NeRF-Real, and DL3DV-Blur. The deblurring prior sharpens textures and edges while maintaining consistent multi-view geometry.

Methods	blurcozy2room			blurfactory			blurpool			blurtanabata			blurwine			Average		
	PSNR↑	SSIM↑	LPIPS↓	PSNR↑	SSIM↑	LPIPS↓	PSNR↑	SSIM↑	LPIPS↓	PSNR↑	SSIM↑	LPIPS↓	PSNR↑	SSIM↑	LPIPS↓	PSNR↑	SSIM↑	LPIPS↓
BAD-Gaussians [22]	22.21	0.673	0.233	19.90	0.652	0.208	22.67	0.545	0.241	16.42	0.428	0.373	16.70	0.477	0.318	19.58	0.555	0.274
Sparse-DeRF* [39]	21.67	0.642	0.253	20.48	0.701	0.185	23.11	0.566	0.218	17.12	0.447	0.381	16.15	0.451	0.323	19.70	0.561	0.272
Difix3D+ [40]	20.57	0.653	0.246	18.31	0.479	0.335	21.11	0.505	0.299	15.89	0.426	0.339	16.24	0.458	0.317	18.46	0.504	0.307
GenFusion [47]	19.75	0.626	0.436	16.65	0.545	0.472	16.42	0.438	0.571	15.21	0.449	0.556	16.17	0.492	0.505	16.84	0.510	0.508
Ours	24.50	0.786	0.131	20.94	0.724	0.174	23.24	0.638	0.210	18.58	0.611	0.231	18.37	0.598	0.230	21.13	0.671	0.195

TABLE VIII: **Quantitative results of novel view synthesis on the synthetic dataset with 3 views.** The per-scene results sum to the average values provided. Each column is colored as: **best** and **second best**.

Methods	blurcozy2room			blurfactory			blurpool			blurtanabata			blurwine			Average		
	PSNR↑	SSIM↑	LPIPS↓	PSNR↑	SSIM↑	LPIPS↓	PSNR↑	SSIM↑	LPIPS↓	PSNR↑	SSIM↑	LPIPS↓	PSNR↑	SSIM↑	LPIPS↓	PSNR↑	SSIM↑	LPIPS↓
BAD-Gaussians [22]	25.61	0.795	0.138	22.62	0.795	0.121	25.64	0.691	0.161	19.09	0.587	0.261	20.43	0.668	0.184	22.68	0.707	0.173
Sparse-DeRF* [39]	23.77	0.754	0.168	22.98	0.815	0.109	25.32	0.694	0.153	19.83	0.708	0.221	19.36	0.638	0.196	22.25	0.722	0.169
Difix3D+ [40]	21.43	0.695	0.210	19.05	0.528	0.314	21.23	0.566	0.275	16.62	0.466	0.335	17.41	0.500	0.299	19.15	0.551	0.287
GenFusion [47]	20.97	0.683	0.386	19.63	0.605	0.447	17.52	0.513	0.513	17.27	0.476	0.535	17.07	0.507	0.498	18.49	0.557	0.476
Ours	26.88	0.843	0.101	23.03	0.842	0.090	26.23	0.735	0.150	21.25	0.736	0.151	21.99	0.762	0.121	23.88	0.784	0.123

TABLE IX: Quantitative results of novel view synthesis on the synthetic dataset with 6 views. The per-scene results sum to the average values provided. Each column is colored as: best and second best.

Methods	blurcozy2room			blurfactory			blurpool			blurtanabata			blurwine			Average		
	PSNR↑	SSIM↑	LPIPS↓	PSNR↑	SSIM↑	LPIPS↓	PSNR↑	SSIM↑	LPIPS↓	PSNR↑	SSIM↑	LPIPS↓	PSNR↑	SSIM↑	LPIPS↓	PSNR↑	SSIM↑	LPIPS↓
BAD-Gaussians [22]	28.45	0.801	0.092	24.38	0.866	0.080	27.05	0.745	0.139	23.34	0.794	0.119	23.92	0.800	0.090	25.43	0.801	0.104
Sparse-DeRF* [39]	25.71	0.768	0.147	23.69	0.833	0.095	25.66	0.714	0.127	20.66	0.737	0.193	20.55	0.679	0.153	23.25	0.746	0.143
Difix3D+ [40]	22.66	0.749	0.183	19.54	0.538	0.317	21.25	0.604	0.254	17.51	0.512	0.318	17.75	0.517	0.301	19.74	0.584	0.275
GenFusion [47]	21.89	0.744	0.341	19.96	0.589	0.474	18.51	0.602	0.439	18.42	0.521	0.525	18.58	0.548	0.481	19.47	0.601	0.452
Ours	29.37	0.899	0.050	25.46	0.891	0.070	27.78	0.789	0.122	24.64	0.837	0.090	24.56	0.841	0.070	26.36	0.851	0.080

TABLE X: Quantitative results of novel view synthesis on the synthetic dataset with 9 views. The per-scene results sum to the average values provided. Each column is colored as: best and second best.

Methods	blurball			blurbuick			blurcoffee			blurdecoration			blurheron			Average		
	PSNR↑	SSIM↑	LPIPS↓	PSNR↑	SSIM↑	LPIPS↓	PSNR↑	SSIM↑	LPIPS↓	PSNR↑	SSIM↑	LPIPS↓	PSNR↑	SSIM↑	LPIPS↓	PSNR↑	SSIM↑	LPIPS↓
BAD-Gaussians [22]	18.59	0.447	0.401	15.88	0.412	0.368	25.70	0.847	0.176	16.75	0.435	0.390	15.96	0.336	0.353	18.58	0.495	0.338
Sparse-DeRF* [39]	18.36	0.374	0.422	15.96	0.398	0.371	23.16	0.708	0.267	16.13	0.477	0.382	15.28	0.357	0.452	17.78	0.463	0.379
Difix3D+ [40]	20.98	0.556	0.363	15.23	0.458	0.471	22.48	0.797	0.233	16.22	0.526	0.523	15.38	0.330	0.485	18.06	0.533	0.415
GenFusion [47]	13.49	0.276	0.642	13.02	0.375	0.543	13.79	0.268	0.610	12.65	0.438	0.573	14.19	0.377	0.575	13.43	0.347	0.589
Ours	19.57	0.525	0.358	16.23	0.493	0.317	26.95	0.868	0.152	17.82	0.535	0.378	17.32	0.457	0.281	19.58	0.576	0.297

TABLE XI: Quantitative results of novel view synthesis on the real-scene dataset with 3 views. The per-scene results sum to the average values provided. Each column is colored as: best and second best.

Methods	blurball			blurbuick			blurcoffee			blurdecoration			blurheron			Average		
	PSNR↑	SSIM↑	LPIPS↓	PSNR↑	SSIM↑	LPIPS↓	PSNR↑	SSIM↑	LPIPS↓	PSNR↑	SSIM↑	LPIPS↓	PSNR↑	SSIM↑	LPIPS↓	PSNR↑	SSIM↑	LPIPS↓
BAD-Gaussians [22]	20.94	0.562	0.311	18.62	0.569	0.271	27.24	0.872	0.143	18.43	0.581	0.299	17.84	0.514	0.264	20.61	0.620	0.258
Sparse-DeRF* [39]	20.62	0.523	0.317	18.16	0.525	0.291	24.32	0.768	0.274	19.16	0.626	0.277	17.75	0.549	0.247	20.01	0.598	0.281
Difix3D+ [40]	21.12	0.565	0.360	17.20	0.510	0.420	24.90	0.844	0.205	17.48	0.553	0.516	16.82	0.397	0.446	19.50	0.574	0.389
GenFusion [47]	18.26	0.488	0.583	17.66	0.566	0.431	15.95	0.385	0.563	12.56	0.489	0.535	15.32	0.438	0.554	15.95	0.473	0.533
Ours	22.31	0.634	0.259	19.98	0.662	0.189	29.77	0.919	0.090	19.26	0.631	0.252	18.69	0.560	0.218	22.00	0.681	0.202

TABLE XII: Quantitative results of novel view synthesis on the real-scene dataset with 6 views. The per-scene results sum to the average values provided. Each column is colored as: best and second best.

Methods	blurball			blurbuick			blurcoffee			blurdecoration			blurheron			Average		
	PSNR↑	SSIM↑	LPIPS↓	PSNR↑	SSIM↑	LPIPS↓	PSNR↑	SSIM↑	LPIPS↓	PSNR↑	SSIM↑	LPIPS↓	PSNR↑	SSIM↑	LPIPS↓	PSNR↑	SSIM↑	LPIPS↓
BAD-Gaussians [22]	22.65	0.648	0.257	19.75	0.567	0.241	28.38	0.888	0.133	20.12	0.666	0.242	19.08	0.529	0.209	22.00	0.660	0.216
Sparse-DeRF* [39]	21.79	0.645	0.297	18.72	0.521	0.290	26.37	0.748	0.166	20.39	0.692	0.227	18.55	0.483	0.231	21.16	0.618	0.242
Difix3D+ [40]	20.57	0.539	0.328	17.97	0.548	0.402	24.92	0.848	0.201	18.39	0.578	0.462	17.08	0.410	0.446	19.79	0.585	0.368
GenFusion [47]	16.92	0.436	0.610	17.57	0.551	0.455	17.08	0.401	0.564	12.97	0.490	0.548	16.41	0.486	0.524	16.19	0.473	0.540
Ours	24.90	0.743	0.220	21.71	0.758	0.142	30.43	0.921	0.086	20.64	0.705	0.194	19.52	0.612	0.193	23.44	0.748	0.167

TABLE XIII: Quantitative results of novel view synthesis on the real-scene dataset with 9 views. The per-scene results sum to the average values provided. Each column is colored as: best and second best.

Methods	0001			0002			0003			0004			0005			Average		
	PSNR↑	SSIM↑	LPIPS↓	PSNR↑	SSIM↑	LPIPS↓												
BAD-Gaussians [22]	15.60	0.513	0.431	15.08	0.484	0.536	14.21	0.389	0.517	12.55	0.517	0.501	17.95	0.602	0.346	15.08	0.501	0.466
Sparse-DeRF* [39]	15.68	0.565	0.412	15.01	0.425	0.560	13.32	0.328	0.511	12.79	0.508	0.497	17.39	0.589	0.527	14.84	0.483	0.501
Difix3D+ [40]	13.90	0.475	0.430	14.71	0.439	0.415	14.66	0.422	0.423	12.88	0.528	0.396	15.66	0.596	0.358	14.36	0.492	0.404
GenFusion [47]	12.11	0.452	0.563	13.24	0.521	0.582	13.68	0.421	0.585	12.34	0.551	0.459	12.73	0.568	0.519	12.82	0.503	0.542
Ours	18.26	0.657	0.322	16.80	0.607	0.434	15.67	0.535	0.489	14.73	0.597	0.378	21.95	0.801	0.217	17.48	0.639	0.368

TABLE XIV: Quantitative results of novel view synthesis on the DL3DV-Blur dataset with 3 views. The per-scene results sum to the average values provided. Each column is colored as: best and second best.

Methods	0001			0002			0003			0004			0005			Average		
	PSNR↑	SSIM↑	LPIPS↓	PSNR↑	SSIM↑	LPIPS↓												
BAD-Gaussians [22]	19.49	0.643	0.289	18.35	0.586	0.359	16.07	0.471	0.432	16.77	0.647	0.309	22.43	0.826	0.176	18.62	0.635	0.313
Sparse-DeRF* [39]	19.35	0.618	0.301	18.61	0.611	0.364	16.11	0.508	0.445	17.11	0.625	0.289	21.90	0.729	0.227	18.61	0.618	0.325
Difix3D+ [40]	16.31	0.552	0.638	16.27	0.519	0.363	14.69	0.421	0.413	14.46	0.604	0.304	15.93	0.597	0.362	15.53	0.538	0.416
GenFusion [47]	15.83	0.605	0.486	17.36	0.621	0.506	14.75	0.463	0.536	16.13	0.616	0.448	18.04	0.740	0.415	16.42	0.609	0.478
Ours	21.89	0.704	0.234	19.06	0.636	0.314	17.32	0.512	0.393	17.46	0.695	0.254	23.77	0.847	0.144	19.90	0.679	0.268

TABLE XV: Quantitative results of novel view synthesis on the DL3DV-Blur dataset with 6 views. The per-scene results sum to the average values provided. Each column is colored as: best and second best.

Methods	0001			0002			0003			0004			0005			Average		
	PSNR↑	SSIM↑	LPIPS↓	PSNR↑	SSIM↑	LPIPS↓												
BAD-Gaussians [22]	22.56	0.733	0.213	18.81	0.617	0.321	17.68	0.525	0.369	17.24	0.633	0.270	22.80	0.845	0.161	19.82	0.671	0.267
Sparse-DeRF* [39]	22.76	0.745	0.235	19.21	0.693	0.291	17.25	0.508	0.386	17.39	0.612	0.278	21.95	0.816	0.196	19.72	0.674	0.277
Difix3D+ [40]	16.95	0.628	0.310	14.86	0.553	0.369	17.30	0.505	0.351	12.99	0.577	0.398	18.69	0.706	0.251	16.16	0.594	0.336
GenFusion [47]	18.87	0.656	0.437	18.11	0.654	0.585	15.70	0.476	0.520	17.83	0.682	0.416	18.67	0.765	0.391	17.84	0.647	0.470
Ours	24.32	0.785	0.177	20.99	0.701	0.266	18.81	0.582	0.332	19.60	0.760	0.211	24.51	0.871	0.129	21.65	0.740	0.223

TABLE XVI: Quantitative results of novel view synthesis on the DL3DV-Blur dataset with 9 views. The per-scene results sum to the average values provided. Each column is colored as: best and second best.